JOURNAL OF COMPUTATIONAL PHYSICS 119, 164–187 (1995)

Spectral Transform Solutions to the Shallow Water Test Set

RUEDIGER JAKOB-CHIEN,* JAMES J. HACK,† AND DAVID L. WILLIAMSON

National Center for Atmospheric Research‡, Boulder, Colorado 80307

Received June 10, 1994; revised December 5, 1994

Solutions to the test case suite proposed by Williamson *et al.* (*J. Comput. Phys.* **102**, 211 (1992)), for the shallow water equations in spherical geometry, are presented. The solutions have been generated using a conventional spectral transform technique combined with a semi-implicit time differencing scheme. For several of the test cases, closed-form solutions do not exist. For these cases, high-resolution numerical integrations of the spectral transform model are used to provide reference solutions against which alternative numerical schemes and lower resolution spectral transform solutions can be evaluated. The sensitivity of the high resolution numerical solutions, associated with temporal truncation, spatial truncation, and internal dissipation, are quantified in order to help bound their uncertainty. In almost all of the test cases, the spectral transform method proves to be a highly accurate solution technique. This is particularly the case at resolutions typically associated with atmospheric general circulation models used to simulate the atmosphere's climate. The most serious deficiency of the spectral transform method, in the context of the test cases, is the introduction of spurious minima and maxima into the solution (caused by Gibbs phenomenon), when sharp gradients exist. Although this behavior is not necessarily a problem for accurately simulating fluid flow, it can become a serious problem for atmospheric general circulation models if the spurious wave structures result in nonphysical states such as negative water vapor mixing ratio.

1. INTRODUCTION

Since the shallow water equations exhibit many of the properties associated with the horizontal dynamical component of three-dimensional atmospheric models, they provide a suitable initial framework for evaluating numerical approximations. A standard test set for evaluating numerical approximations to the shallow water equations in spherical geometry has been proposed by Williamson *et al.* [17]. The test suite is designed to evaluate numerical methods proposed for global atmospheric general circulation models and to identify the merits of any trade-offs that might be faced in their implementation. This paper presents a summary of solutions to the proposed test cases obtained using the spectral transform method. We do not report on the formulation of the numerical test set, but instead rely on [17] to provide a detailed mathematical description of the test cases and the requested performance metrics.

The global atmospheric modeling community has long understood that the adaptation and development of computational methods for solving partial differential equations in spherical geometry is complicated by the unique characteristics of the coordinate system itself. For example, since longitude is multivalued at the pole, non-zero vector functions will have multivalued or discontinuous components, even though the same functions have smooth properties in a Cartesian framework. As another example, the use of a uniformly distributed latitude–longitude finite-difference grid requires either an excessively small time step (to satisfy the local linear stability criteria) or some form of empirical filtering of longitudinal waves near the poles because of the convergence of longitude lines. Such difficulties, which are uniquely associated with the spherical coordinate system, are collectively referred to as the "pole problem." The spectral method presents a natural solution to problems introduced by spherical geometry in part because it provides an isotropic representation in wavenumber space even though the commonly adopted underlying Gaussian grids do not. The spectral transform method, which made spectral methods competitive with finite-difference approaches in terms of storage and processor time, was first introduced by Orszag [10] and Eliasen *et al.* [3]. A fairly complete discussion of the history and algorithmic properties of the spectral transform procedure can be found in Bourke *et al.* [2] and Machenhauer [11]. Although not universally adopted, the method is now widely accepted as the basis for both operational numerical weather prediction and global climate modeling.

The solutions summarized in this paper and presented in detail in Jakob *et al.* [8] were generated using a semi-implicit spectral transform based shallow water model, where the specific algorithms and numerical approximations are described in Hack and Jakob [6]. An overview of the governing equations, including generalizations to accommodate several of the test cases, is provided in Section 2. Details associated with the code implementation affect the calculated error measures in those test cases that are trivial for the spectral method. In particular, the degree of orthogonality of the discrete polynomials and Gaussian quadrature is several orders of magnitude above ma-

* Current affiliation: Department of Computer Science, University of Northern Iowa, Cedar Falls, IA 50615-0507.

† Corresponding author.

‡ The National Center for Atmospheric Research is sponsored by the National Science Foundation.

0021-9991/95 $6.00

chine rounding levels. This is quantified in Section 2 so as to explain the observed results in these cases, although it is basically irrelevant for practical applications. In some cases and, in particular, Test Case 7 involving atmospheric initial conditions, spurious gravity waves can contaminate the solutions. In such cases, an initialization step is desirable to minimize the mass and momentum imbalances in the initial condition. The initialization procedure used for Test Case 7 is also described in Section 2. Solutions to Test Cases 1–4, for which analytic solutions exist, are discussed in Section 4. The remaining test cases, zonal flow over an isolated mountain (Test Case 5), Rossby–Haurwitz wave (Test Case 6), and analyzed 500 mb height and wind field initial conditions (Test Case 7), do not have closed-form solutions. In order to evaluate the performance of alternative numerical methods for these test cases, high resolution reference solutions have been computed using the spectral transform model. The sensitivity of these solutions to arbitrary parameters such as the time step, diffusion coefficient, and the number of modes retained in the numerically generated reference data sets are discussed in Section 3 to indicate their uncertainty. The reference solutions themselves and lower resolution approximations are discussed in Section 5.

Because of the sheer volume of performance metrics requested with the test cases, we include only an abbreviated discussion of the spectral transform solutions in this paper. A more complete discussion of the spectral transform results, including all of the performance metrics requested in [17] is provided in the technical report by Jakob *et al.* [8]. Copies of this technical report may be obtained from Hack or Williamson at NCAR (jhack@ncar.ucar.edu; wmson@ncar.ucar.edu).

2. GOVERNING EQUATIONS AND SOLUTION METHOD

Governing Equations

In vector form, the horizontal momentum and mass continuity equations governing the behavior of a rotating, homogeneous, incompressible, and hydrostatic fluid are written as

$$\frac{d\mathbf{V}}{dt} = -f\mathbf{k} \times \mathbf{V} - \nabla\Phi, \tag{2.1}$$

and

$$\frac{d\Phi}{dt} = -\Phi\nabla \cdot \mathbf{V}, \tag{2.2}$$

where $\mathbf{V} \equiv \mathbf{i}u + \mathbf{j}v$ is the horizontal (with respect to the surface of the sphere) vector velocity, $\Phi \equiv gh$ is the free surface geopotential, h is the free surface height, g is the acceleration of gravity, $f \equiv 2\Omega \sin\phi$ is the Coriolis parameter, ϕ denotes latitude, and Ω is the angular velocity of the earth. The substantial derivative is given by

$$\frac{d}{dt}(\quad) = \frac{\partial}{\partial t}(\quad) + (\mathbf{V} \cdot \nabla)(\quad), \tag{2.3}$$

and the ∇ operator is defined in spherical coordinates as

$$\nabla(\quad) \equiv \frac{\mathbf{i}}{a\cos\phi}\frac{\partial}{\partial\lambda}(\quad) + \frac{\mathbf{j}}{a}\frac{\partial}{\partial\phi}(\quad), \tag{2.4}$$

where λ denotes longitude and a is the radius of the earth.

The solutions to the test cases presented here are obtained from a spectral transform code described in Hack and Jakob [6] which approximates these equations. Test Case 5, however, uses an irregular lower boundary (i.e., surface topography) requiring changes to the generic form of the shallow water equations in [6] and above. Additionally, several of the "nonlinear" test cases exhibit an unforced energy cascade from low to high wavenumber. A dissipation process is generally employed to deal with the accumulation of energy at the truncation limit, sometimes referred to as spectral blocking, by mimicking horizontal mixing that occurs on smaller, unresolved scales of motion. Consequently, a diffusion operator of the type typically applied in atmospheric general circulation models is included in the governing equations for Test Cases 5, 6, and 7. This process is especially important for the lower resolution model integrations where even the initial data can have significant energy near the truncation limit. Thus, the prediction equations (2.1) and (2.2) must be generalized to provide for surface topography and to include a parameterization of subgrid-scale mixing in the form of a dissipation term.

Let h_s denote the height of the mountains, h^* the depth of the fluid, and $h = h^* + h_s$ the height of the free surface. In the momentum equation (2.1) the pressure gradient force continues to be based on the gradient of the free surface

$$\frac{d\mathbf{V}}{dt} = -f\mathbf{k} \times \mathbf{V} - \nabla(\Phi_s + \Phi^*) + F_{\mathbf{V}}^{\text{Diff}}, \tag{2.5}$$

where the surface geopotential $\Phi_s = gh_s$ and $\Phi^* = gh^*$. The mass continuity equation (2.2), however, applies only to the depth of the fluid, taking the form

$$\frac{d\Phi^*}{dt} = -\Phi^*\nabla \cdot \mathbf{V} + F_{\Phi}^{\text{Diff}}. \tag{2.6}$$

In each of these equations an internal dissipation term has also been included.

As in [6], the geopotential Φ^* is divided into a time-invariant spatial mean $\overline{\Phi}$ and a time-dependent deviation $\Phi' = \Phi^* - \overline{\Phi}$. After applying the *curl* and *div* operators, the absolute vorticity, divergence, and geopotential prediction equations become

$$\frac{\partial\eta}{\partial t} = -\frac{1}{a(1-\mu^2)}\frac{\partial}{\partial\lambda}(U\eta) - \frac{1}{a}\frac{\partial}{\partial\mu}(V\eta) + F_{\eta}^{\text{Diff}}, \tag{2.7}$$

$$\frac{\partial \delta}{\partial t} = \frac{1}{a(1-\mu^2)}\frac{\partial}{\partial \lambda}(V\eta) - \frac{1}{a}\frac{\partial}{\partial \mu}(U\eta) - \nabla^2\left(\Phi_s + \Phi' + \frac{U^2+V^2}{2(1-\mu^2)}\right) + F_\delta^{\text{Diff}}, \tag{2.8}$$

$$\frac{\partial \Phi'}{\partial t} = -\frac{1}{a(1-\mu^2)}\frac{\partial}{\partial \lambda}(U\Phi') - \frac{1}{a}\frac{\partial}{\partial \mu}(V\Phi') - \overline{\Phi}\delta + F_\Phi^{\text{Diff}}, \tag{2.9}$$

where the absolute vorticity $\eta \equiv (\mathbf{k} \cdot \nabla \times \mathbf{V}) + f = \zeta + f$, the divergence $\delta \equiv (\nabla \cdot \mathbf{V})$, and $\mu \equiv \sin \phi$. Note that the generalized equations include the surface topography term Φ_s only in the divergence tendency equation. The changes to the numerical algorithm are thus relatively small. Only the definition of the intermediate variable E in (5.11) of [6] must be changed to

$$E \equiv \Phi_s + \frac{U^2+V^2}{2(1-\mu^2)}. \tag{2.10}$$

The form of the dissipation terms is equivalent to the horizontal diffusion used in the NCAR Community Climate Models [16, 7] and is given by

$$F_\eta^{\text{Diff}} = -K_4[\nabla^4\eta - \frac{4}{a^4}\eta], \tag{2.11}$$

$$F_\delta^{\text{Diff}} = -K_4[\nabla^4\delta - \frac{4}{a^4}\delta], \tag{2.12}$$

$$F_\Phi^{\text{Diff}} = -K_4\nabla^4(\overline{\Phi} + \Phi' + \Phi_s). \tag{2.13}$$

The linear correction term has been added to the diffusion operators in the vorticity and divergence equations to prevent the damping of solid body rotation. The geopotential diffusion operator is applied to the free surface geopotential so as not to cause spurious damping associated with surface topography. The linear diffusion operator is implicitly evaluated (i.e., after the spectral coefficients for the new time level have been updated by a dynamical time step) in spectral space since the spectral form of the ∇^4 operator is a trivial algebraic relationship.

Solution Method

The original implementation of the spectral transform method employed for the solutions in this report is detailed in [6]. The modifications required for the inclusion of surface topography and internal dissipation are detailed in [8]. The spectral transform algorithm relies on both grid- and spectral-based representations of the predicted variables. For an arbitrary variable ψ, grid values are related to spectral coefficients by

TABLE I

Spectral Transform Grid Resolution

Spectral truncation M	Number of grid points	
	Meridional: J	Longitudinal: I
42	64	128
63	96	192
106	160	320
170	256	512
213	320	640

$$\psi(\lambda, \mu) = \sum_{m=-M}^{M}\sum_{n=|m|}^{\mathcal{N}(m)} \psi_n^m P_n^m(\mu) e^{im\lambda}, \tag{2.14}$$

where $P_n^m(\mu)e^{im\lambda}$ are the spherical harmonic functions used for the expansion basis (where $P_n^m(\mu)$ are the associated Legendre functions), M is the highest fourier wavenumber included in the east–west representation, and $\mathcal{N}(m)$ is the highest degree of the associated Legendre functions for longitudinal wavenumber m. In the grid representation, ψ is given at discrete latitudes λ_i and longitudes μ_j, with $1 \le i \le I$ and $1 \le j \le J$.

The coefficients of the spectral representation (2.14) are determined by

$$\psi_n^m = \int_{-1}^{1}\frac{1}{2\pi}\int_0^{2\pi}\psi(\lambda, \mu)e^{-im\lambda}\,d\lambda P_n^m(\mu)\,d\mu. \tag{2.15}$$

The inner integral represents a Fourier transform,

$$\psi^m(\mu) = \frac{1}{2\pi}\int_0^{2\pi}\psi(\lambda, \mu)e^{-im\lambda}\,d\lambda, \tag{2.16}$$

which is evaluated using a fast Fourier transform (FFT) routine. The outer integral is evaluated using Gaussian quadrature,

$$\psi_n^m = \sum_{j=1}^{J}\psi^m(\mu_j)P_n^m(\mu_j)w_j, \tag{2.17}$$

where μ_j denotes the Gaussian grid points in the meridional direction and w_j is the Gaussian weight at point μ_j.

All solutions presented in the following have been computed using triangular spectral truncations, $\mathcal{N}(m) = M$, which have become the most comonly adopted spectral truncation due to the isotropic nature of the underlying spectral representation. Consequently, the spectral transform process cannot contribute to asymmetries in otherwise symmetric solutions. Alternative truncation strategies, such as rhomboidal truncation, are generally used for extremely low resolution models, and are not considered here. Table I lists the spectral truncations employed in the following numerical experiments and the corresponding

TABLE II

Diffusion Coefficient K_4 as a Function of Spectral Truncations

Spectral truncation	K_4 (m^4/s)
42	0.50×10^{16}
63	1.00×10^{15}
106	1.25×10^{14}
170	2.00×10^{13}
213	8.00×10^{12}

number of meridional and longitudinal points for the transform grid. The longitudinal distribution of the grid points is equiangular, while the meridional distribution is nearly equiangular. The meridional grid points are located at the Gaussian latitudes θ_j, which are the J roots of the Legendre polynomial: $P_J(\sin\theta_j) = 0$. The number of grid points in the longitudinal and meridional directions are determined so as to allow the unaliased representation of quadratic terms,

$$I \geq 3M + 1, \tag{2.18}$$

$$J \geq (3N + 1)/2, \tag{2.19}$$

where N is the highest wavenumber retained in the latitudinal Legendre representation ($N = \max\{(\mathcal{N}m)\} = M$ in the case of triangular truncation). Furthermore, the implementation in [6] requires an even number of latitudes to make convenient use of the hemispheric symmetry of the associated Legendre functions. The number of longitudes are also constrained to have only the prime factors 2, 3, and 5 to allow the use of the highly efficient FFT library developed by Temperton [14].

Table II lists values of the diffusion coefficients K_4 that have been used as a function of triangular wavenumber truncation for the solutions illustrated in later sections (unless specifically stated otherwise). The coefficients scale as $[N(N + 1)]^{-2}$ so that the smallest scales (highest wavenumber) are damped at approximately the same rate. The effect of diffusion on the solutions is discussed in some detail in the next section.

Table III lists the time steps that have been used to produce the solutions presented in later sections, unless specifically stated otherwise in the text. The time step scales approximately as $1/N$ for reasons associated with linear stability.

The global integral (Eq. (81) in [17]), used in many of the requested error measures,

$$I(h) = \frac{1}{4\pi}\int_0^{2\pi}\int_{-\pi/2}^{\pi/2} h(\lambda, \theta)\cos\theta\, d\theta\, d\lambda, \tag{2.20}$$

is approximated consistently with the Gaussian quadrature of the spectral transform method (2.14), by the discrete double sum

$$I(h) \approx \frac{1}{2I}\sum_{i=1}^{I}\sum_{j=1}^{J} h(\lambda_i, \theta_j)w_j, \tag{2.21}$$

where w_j are the weights of the Gaussian quadrature.

The most commonly requested error measures are normalized l_1, l_2, and l_∞ norms. Using the height field as an example, where h_T is the true solution, these metrics are defined as

$$l_1(h) = \frac{I[|h(\lambda, h) - h_T(\lambda, \theta)|]}{I[|h_T(\lambda, \theta)|]}, \tag{2.22}$$

$$l_2(h) = \frac{\{I[(h(\lambda, \theta) - h_T(\lambda, \theta))^2]\}^{1/2}}{\{I[h_T(\lambda, \theta)^2]\}^{1/2}}, \tag{2.23}$$

$$l_\infty(h) = \frac{\max_{\text{all}\lambda,\theta}|h(\lambda, \theta) - h_T(\lambda, \theta)|}{\max_{\text{all}\lambda,\theta}|h_T(\lambda, \theta)|}. \tag{2.24}$$

Additional details can be found in [17]. A discussion of the effects of grid sampling and spectral truncation is included later in this paper.

An optional Asselin time filter, which is part of the spectral shallow water model implementation (as discussed in [6]), has not been used for the solutions presented here, unless specifically stated otherwise. No significant even–odd temporal mode splitting was observed in any of the solutions, even those that made use of extended integration periods.

Initialization

As mentioned earlier, Test Case 7 consists of a set of numerical integrations that start from analyses of observed data. Because the observational data are either incomplete, imperfect, or both, analysis procedures can alias the slow atmospheric motions onto fast gravity-wave type motions. These aliased waves often have relatively large (unrealistic) amplitudes in model forecasts, but they can be eliminated by modifying the initial data with specialized initialization procedures. The initial data for Test Case 7 have been modified accordingly. The unmodified initial data were obtained from European Center for Medium Range Weather Forecasts (ECMWF) analyses, as compiled by Trenberth and Olson [15]. These data are available

TABLE III

Model Time Step as a Function of Truncation

Spectral truncation	Timestep (seconds)
42	1200
63	900
106	600
170	450
213	360

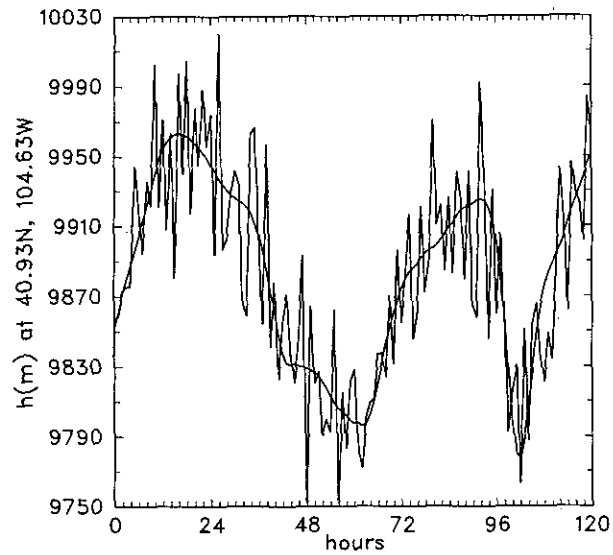

FIG. 2.1. Height time series without (noisy) and with (smooth) nonlinear normal mode initialization at the grid point closest to (40°N, 105°W).

as grid point values on a T42 Gaussian grid. However, the point values were interpolated from the ECMWF data archive using cubic splines (i.e., they were not spectrally truncated at T42) and thus contain waves up to T63. A 10-km mean height for the 500-mb equivalent geopotential was assumed for these test cases. The data were then initialized using a Machenhauer nonlinear normal mode initialization (NNMI) with Hough functions appropriate for a 10-km equivalent depth. After an initial linear step zeroing the gravity wave amplitudes, five iterations of the NNMI were used. This procedure has been described by Errico [4] and Errico and Eaton [5] for the NCAR Community Climate Model. The actual initialization code for the shallow water model was provided by Andy van Tuyle (personal communication, 1992).

Figure 2.1 shows the height time series for a point near Boulder, Colorado (40°N,105°W) computed from the uninitialized data and from the initialized data. A comparison shows that the high frequency variations in the height field have been filtered out without changing the lower frequency, synoptic-scale features of the flow.

Implementation Aspects

For a few of the test cases, where the spectral transform method is expected to be accurate to rounding levels, a large component of the error in our solutions is associated with the discrete computational non-normality and non-orthogonality of the basis functions. Although this is of little consequence for practical applications, we review the source of the discrepancies that will be seen later. The codes that generated the associated Legendre functions used in the tests produce functions with orthogonality and normality errors that can be as large as $1000\,\varepsilon$, where ε is machine accuracy (1.4×10^{-14} in the case of CRAY floating point format). The largest orthogonality and normality errors are given in Table IV for the resolutions included in this study. These errors are defined as the largest Gaussian quadrature of any associated Legendre function with any other of same order m, and the largest of one minus the quadrature of any function with itself. The errors are not equally distributed, but they are particularly large for spherical harmonic modes with relatively large degree n and orders $m = 0$ and $m = 1$.

As would be expected, the orthonormality errors are reduced using double precision arithmetic for the calculation of the Gaussian latitudes, weights, and Legendre functions. At T42 the maximum orthogonality and normality errors are reduced to 8.0×10^{-14} and 2.2×10^{-13}, respectively, when the latitudes and weights are calculated in double precision, and to 3.5×10^{-14} and 6.8×10^{-14}, respectively, when the polynomials are also calculated in double precision. In both cases, the quadrature remains a single precision operation so that the orthonormality is still not to machine accuracy because of rounding error in the quadrature itself.

Performance Measures

Finally, sequential and parallel performance results for the shallow water code (see the Appendix) on the Cray Y-MP vector multiprocessor can be found in Jakob [9], which also includes a performance model for the spectral transform algorithm and its implementation. Table V contains representative execution times and execution rates for a semi-implicit time step as a function of model resolution for Test Case 2. The effects of the $O(n^3)$ growth in operation count associated with the Legendre transform (a well-known problem with global spectral models) can be seen in this table. The T213 operation count is approximately 80 times larger than at T42, and overall it is less than half as efficient in terms of the number of available degrees of freedom.

3. SOURCES OF REFERENCE SOLUTION UNCERTAINTY

Test Cases 5–7 do not have analytic solutions. Therefore, it is necessary to generate reference solutions using a very high

TABLE IV

Computational Error in Spherical Harmonic Basis, Expressed as the Maximum Difference between the Computational and Analytic Scalar Product

Resolution	Orthogonality	Normality
T42	9.0×10^{-12}	8.5×10^{-12}
T63	1.7×10^{-11}	1.6×10^{-11}
T106	8.5×10^{-11}	8.5×10^{-11}
T213	3.2×10^{-10}	3.2×10^{-10}

TABLE V

Representative CPU Time (Seconds) and Floating Point Execution Rate (in Millions of Floating Point Operations per second or MFLOPS) on a Single CRAY Y-MP Processor per Semi-implicit Time Step as a Function of Horizontal Spectral Resolution

Spectral truncation	T42	T63	T106	T170	T213
Execution time	0.019	0.053	0.184	0.598	1.140
Execution rate	162	169	198	214	215

Note. The execution time for a 1-day integration can be obtained by combining this data with the time step data in Table III.

resolution version of the spectral transform model. Since these are also only approximate solutions, it is desirable to have some estimate of their uncertainty. In this section, we present various properties of the real data forecasts (Test Case 7) with the high resolution version of spectral shallow water model to illustrate the uncertainties associated with using such integrations as reference solutions. In particular, we examine the uncertainty associated with the incorporation of dissipation in the governing equations. Certainly, errors smaller than the difference in the reference solutions with and without internal dissipation indicates that a test solution is within the uncertainty of the reference solution, and any solution reasonably close to the reference solution should also be considered as within the uncertainty. The uncertainties determined by these tests represent a minimum level of uncertainty. For complete reliance on these reference solutions, similar solutions must be obtained using other numerical approximations applied at high resolution. Until such solutions are produced, the reference solutions presented here should be used cautiously. All numerical reference solutions presented in this paper were determined using a T213 spectral truncation, currently the highest wavenumber truncation employed in operational forecast models. Limited tests at T426 indicate additional convergence above T213 which marginally affects the details of the results, where the differences are considerably smaller than the uncertainty associated with temporal truncation, diffusion, and truncation to T106 (as discussed in the latter part this section).

Kinetic Energy Considerations for Internal Dissipation

As mentioned in [17], the addition of an explicit diffusion term may be desirable for several of the test cases and may lead to improvement in some of the error measures. We begin this discussion by defining the specific kinetic energy per volume element as

$$KE = \tfrac{1}{2}\mathbf{V} \cdot \mathbf{V}. \tag{3.1}$$

As shown in [8], assuming triangular truncation ($\mathcal{N}(m) = M$), the global mean of the specific kinetic energy $\overline{KE}_n$ for spherical wavenumber $1 \le n \le M$ can be written in terms of divergence and vorticity spectral coefficients as

$$\overline{KE}_n = \frac{a^2}{4n(n+1)}\left[\zeta_n^0(\zeta_n^0)^* + \delta_n^0(\delta_n^0)^* + 2\sum_{m=1}^{n}\zeta_n^m(\zeta_n^m)^* + 2\sum_{m=1}^{n}\delta_n^m(\delta_n^m)^*\right]. \tag{3.2}$$

Figure 3.1a shows the kinetic energy spectra from day 5 of two T213 forecasts using the 21 December 1978 initial data of Test Case 7 with (lower curve) and without (upper curve) diffusion. The diffusion coefficient was chosen to give a reasonably straight tail to the energy spectra. For the coefficient chosen, the tail is slightly steeper than the -3 slope line plotted for reference. This plot shows that the diffusion has no discernable effect on wavenumbers less than 40.

Figure 3.1b shows the energy spectra from T106 integrations with and without diffusion using the 21 December 1978 initial data of Test Case 7. For these experiments, there is no discernable difference for wavenumbers less than 15. Figures 3.1c and d compare the energy spectra from the T106 and T213 forecasts without and with diffusion, respectively. In both cases, although the low wavenumber behavior is very similar, there are observable differences in wavenumbers as small as 8. For these particular diffusion coefficients, the characteristics of the T106 forecast spectrum are very similar to the T213 forecast spectrum. There is less similarity with either the T63 and T42 spectra when compared to the T213 results. This comparison is shown in Figures 3.1e and f for the T63 and T42, respectively. The tail in both curves is slightly steeper than the corresponding portion of the T213 energy spectrum, indicating that the magnitude of the dissipation could probably be reduced.

Dependence of the Error Measures on Parameters Defining the Reference Solution

We have performed several numerical experiments to quantify the uncertainty in the reference solutions due to the choice of values for some of the arbitrary parameters. These experiments indicate that the reference solution can be no better than the differences indicated but they do *not* indicate that it is necessarily as good as these differences. The differences are summarized in Table VI. All experiments were conducted using a T213 truncation and the 21 December 1978 initial data set in Test Case 7. The first experiment compares the solution truncated to T106 with the complete T213 representation and illustrates the component of the error norm attributable to the neglect of waves 107 through 213. The second experiment compares the forecasts with and without diffusion and illustrates the uncertainty introduced by explicit internal dissipation. The third experiment compares the standard 360-s time step with a 450-s time step, providing some indication of the role of the time truncation error.

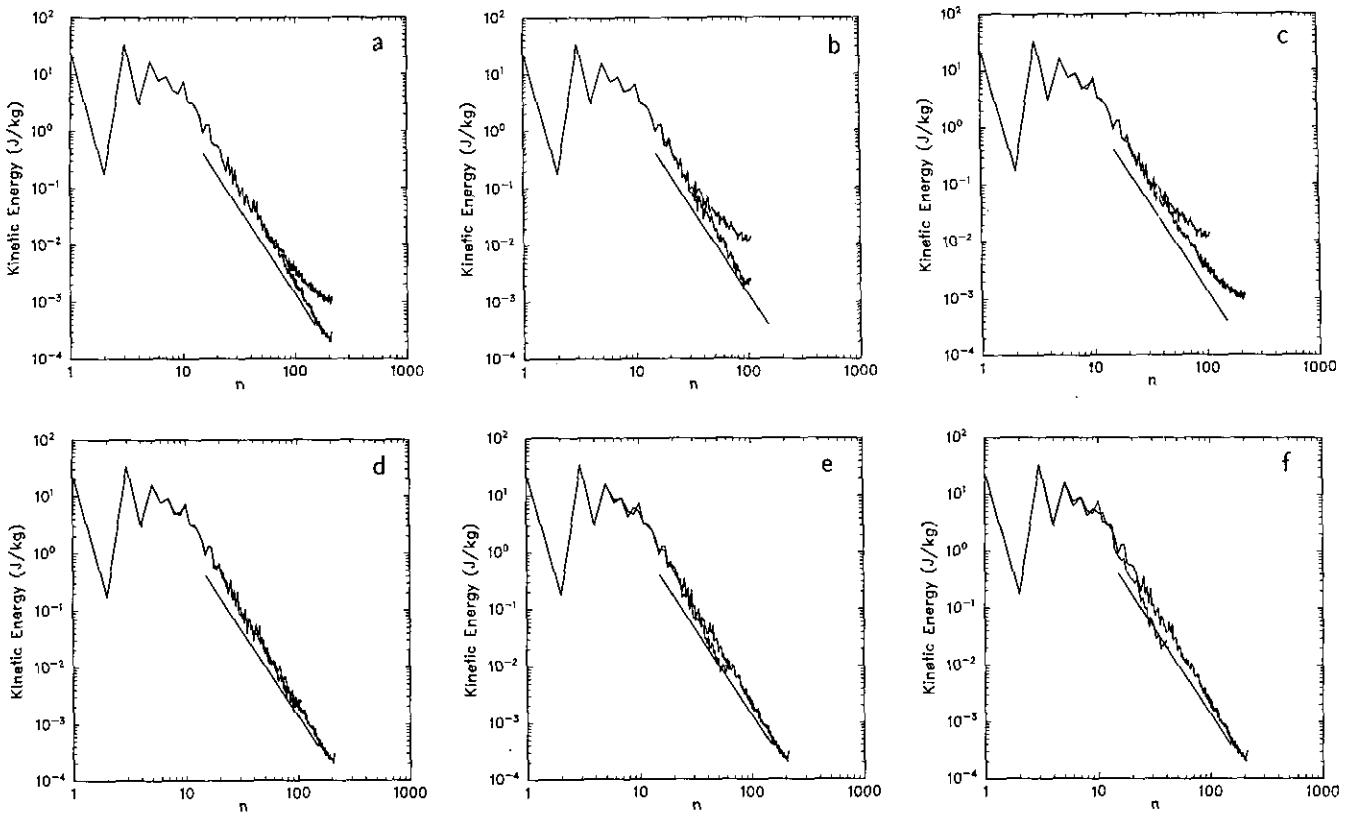

FIG. 3.1. Kinetic energy spectra for day 5 of forecasts from 21 December 1978 initial data: (a) T213 resolution with (lower curve) and without (upper curve) diffusion; (b) T106 with (lower curve) and without (upper curve) diffusion; (c) T213 and T106 without diffusion; (d) T213 and T106 with diffusion; (e) T213 and T63 with diffusion; (f) T213 and T42 with diffusion. The straight line in all panels has a -3 slope.

Any errors calculated with respect to the high resolution reference solution, that are smaller than errors included Table VI, indicate only that the alternate numerical scheme produces results within the uncertainty of the reference solution.

The Effect of Diffusion on Error Measures

Figure 3.2 compares the normalized $l_2(h)$ errors for the T106 solutions from the 21 December 1978 initial data of Test Case 7 with (solid) and without (dashed) diffusion. They are evaluated against the T213 reference solution with diffusion, retaining all 213 waves in the grid representation. The differences in the

TABLE VI

Approximation Differences after 5 Days

	l_1(h)	l_2(h)	l_∞(h)
Difference due to 106 truncations	1.0×10^{-5}	2.0×10^{-5}	2.5×10^{-4}
Difference due to diffusion	8.0×10^{-5}	1.5×10^{-4}	2.5×10^{-3}
Difference due to time step	3.5×10^{-5}	5.5×10^{-5}	6.0×10^{-4}

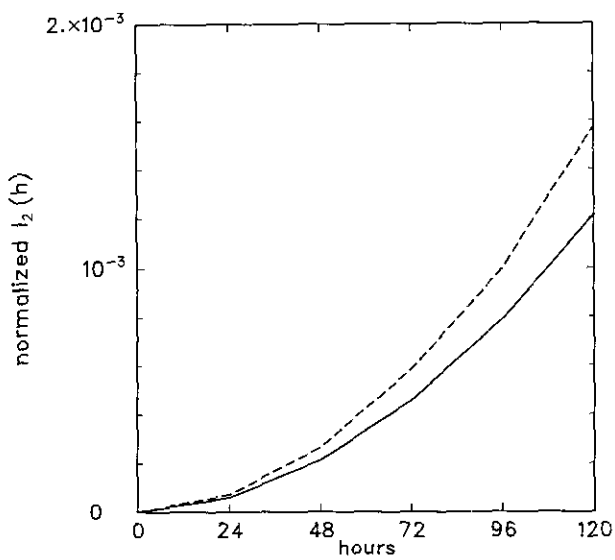

FIG. 3.2. l_2, height errors for T106 resolution from 21 December 1978 initial data without (dashed) and with (solid) diffusion.

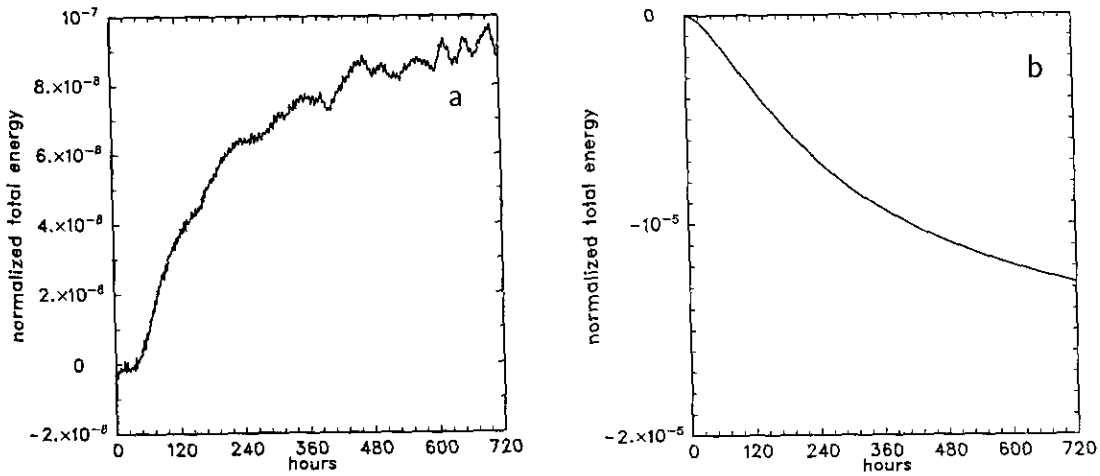

FIG. 3.3. Normalized total energy (a) without and (b) with diffusion for T213 resolution from 21 December 1978 initial data.

normalized l_1, l_2, and l_∞ norms (where the l_1 and l_∞ curves are not shown) grow to 1.8×10^{-4}, 3.6×10^{-4}, and 2.2×10^{-3}, respectively, by day five of the forecast. The diffusion decreases the errors slightly by damping the erroneous small scales. This damping is evident in the kinetic energy spectra shown earlier. Any alternative numerical scheme with error norms in this range should probably be considered to be comparable to a T106 spectral solution.

The Effect of Diffusion on Global Integrals

When diffusion is included in the shallow water equations, mass, vorticity and divergence continue to be conserved by the continuous equations, whereas energy and enstrophy are no longer conserved quantities. In what follows, we present the global integrals from 30 day integrations using a T213 truncation with and without diffusion. Normalized mass is conserved to nine digits over the 30-day period. The global average vorticity grows no larger than $5 \times 10^{-14}\, s^{-1}$ over the 30 days without diffusion, becoming almost three times larger by the end of the 30-day period when diffusion is included. Global average divergence behaves similarly in the two cases (i.e., independent of the diffusion term), growing to $-4 \times 10^{-16}\, s^{-1}$ by the end of the integration period. Figures 3.3a and b show the normalized total energy without and with diffusion. Without diffusion (a) the energy remains conserved to seven digits, whereas with diffusion (b) it is conserved to only five digits and decreases as would be expected. Normalized potential enstrophy remains conserved to four digits without diffusion and slightly better than one digit with diffusion, again decreasing as expected.

The Effect of Neglecting Waves 107 through 213 of the Reference Solution

Table VI above indicates the uncertainty in the reference solution due to the neglect of waves 107 through 213. The errors in the T106 solution are large enough that for practical purposes they can be determined using the T213 solution truncated to T106. The normalized l_1 error graphs (not shown) for the two cases are indistinguishable from each other as are those for the l_2 error. The largest difference occurs with the normalized $l_\infty(h)$ error shown in Fig. 3.4 in which the solid line is from the complete T213 solution and the dashed line is from the T213 solution truncated to T106.

The Effect of Time Step on Error

The errors in the unforced T106 solutions are dominated by spatial truncation error, not by temporal truncation error. Figure

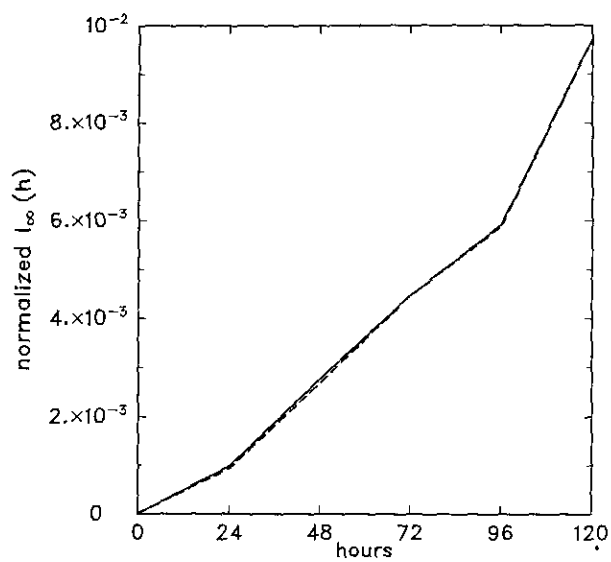

FIG. 3.4. l_∞ height difference of 5-day T106 integration (using 21 December 1978 initial data) compared to T213 reference solution truncated to T106 (dashed).

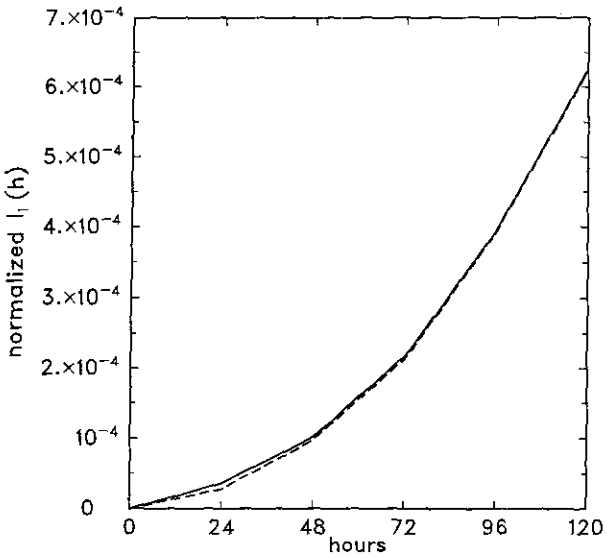

FIG. 3.5. l_1 height error for T106 integration of 21 December 1978 initial data with 600-s (solid) and 300-s (dashed) time steps.

3.5 shows the normalized $l_1(h)$ error norm for the T106 solution with the standard 600-s time step (solid) and with a 300-s step (dashed). Of all the error norms, the l_1 metrics show the largest difference, while the two normalized l_2 norms are indistinguishable from each other, as are the two l_∞ norms.

4. TEST CASES 1–4

In this and the next section, we summarize the solution errors using the spectral transform method applied at resolutions currently favored by climate modeling applications. Complete details and additional explanation of these results are provided in [8]. The reader is referred to [17] for complete descriptions of the test cases themselves, their associated error measures, and the values for all physical constants. Test Cases 1–4 each have analytic solutions. Thus, they provide an exact reference for validating numerical solution techniques, including the spectral transform method. These test cases fall into two categories in the context of the spectral transform method. Test Case 2 (global steady state nonlinear zonal geostrophic flow) and Test Case 3 (steady state nonlinear zonal geostrophic flow with compact support) are trivially handled by the spectral transform technique, while Test Case 1 (advection of a cosine bell over the pole) and Test Case 4 (forced nonlinear system with a translating low) require considerably higher spectral truncation for comparably accurate solutions. The trivial cases are considered first.

Test Case 2—Zonal Geostrophic Flow

The global zonal geostrophic flow case is a trivial problem for the spectral transform method since the height and wind fields can be represented exactly by the basis functions of degree $n \leq 1$. Errors in the numerical solution reflect the accumulation of rounding errors associated with our particular spectral transform implementation and computer system, rather than truncation errors associated with the spectral method. Consequently, there is no point in performing a study of solution convergence as a function of horizontal resolution for this case. Figure 4.1 shows the l_2 height errors, using a T42 spectral resolution for each of the four rotation angles. The solid line is for $\alpha = 0$ and for $\alpha = 0.05$, while the dashed line is for $\alpha = \pi/2 - 0.05$, and for $\alpha = \pi/2$ (where α is the angle between the pole of the computational grid and the axis about which geostrophic flow takes place). As a general rule, the h error norms for the $\alpha = 0.0$ and 0.05 cases are very close to each other and in many instances are indistinguishable (as in Fig. 4.1). The $\alpha = \pi/2$ and $\pi/2 - 0.05$ error norms are also generally close to each other, but with smaller amplitude than the other pair of rotation angles. The wind errors exhibit similar characteristics. In general, the error norms associated with this test case are extremely small, and there is clearly no need for alternative numerical schemes to do as well on this test case to be considered viable for atmospheric modeling applications.

With $\alpha = 0.0$ and 0.05 the spatial distribution of the solution error is concentrated near the representational poles and coincident, or nearly coincident, with the rotational poles (we define the representational pole to be the pole associated with the spectral representation or computational grid, and the rotational pole to be associated with the rotating geometry of the physical problem). When the representational pole is near the rotational equator ($\alpha = \pi/2$ and $\pi/2 - 0.05$) the errors are more evenly distributed. An examination of the errors associated with the spectral truncation of the initial condition shows that in all

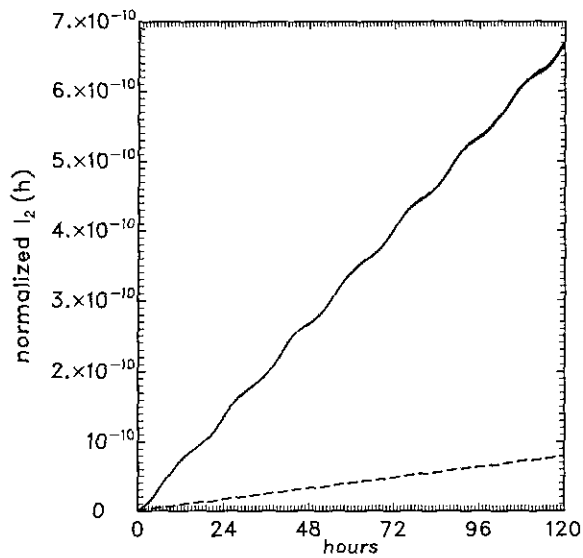

FIG. 4.1. l_2 height error for T42, zonal geostrophic flow case. Thick solid for $\alpha = 0$, thin solid for $\alpha = 0.05$, thin dashed for $\alpha = \pi/2 - 0.05$, and thick dashed for $\alpha = \pi/2$.

cases the errors are associated with the representational pole and are primarily related to the discrete computational non-normality and non-orthogonality of the polynomials (as discussed in Section 2.)

Test Case 3—Zonal Geostrophic Flow with Compact Support

Test case 3, zonal geostrophic flow with compact support, is also a trivial problem for the spectral transform method at resolutions commonly in use today. Over the 5-day integration period, the errors are primarily the result of truncation error as opposed to the previous case where they were the result of a lack of orthogonality to rounding levels of the basis functions at T42. Initially, the errors are only one order of magnitude larger for the height field and two orders of magnitude larger for the wind field than the discrete orthonormality errors discussed in Section 2. Thus, they are insignificant with regard to practical problems. As with Test Case 2, alternative numerical schemes do not have to perform as well to be considered viable for practical applications. Figure 4.2 shows the l_2 height errors for the T42 case using $\alpha = 0$ (wide solid line) and $\alpha = \pi/3$ (dashed line) along with the T63 case for $\alpha = \pi/3$ (narrow solid line). Compared to the global scale zonal flow case (Test Case 2), the T42, $\alpha = 0$ height errors are larger initially; then they grow as they do in Test Case 2. When $\alpha = \pi/3$, the height errors are larger in the compact support case than in the global case for the entire period, since the global case shows slow growth for the 5-day period. The noise superimposed on the T42 curves is believed to be attributable to the lack of initialization for this integration. Very small amplitude gravity waves are present due to small errors in the evaluation of the integral used to determine the balanced height field. These waves propagate meridionally (as defined by the rotational pole, rather than the representational pole) and are present to the same extent in the both the $\alpha = 0$ and $\alpha = \pi/3$ cases. The observed noise results from discrete sampling of these waves as their maxima and minima fall near and between the discrete transform grid

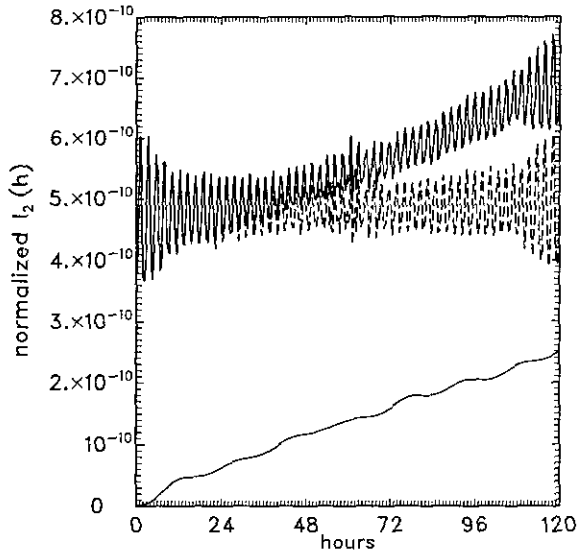

FIG. 4.2. l_2 height error for Test Case 3. Wide solid line for T42, $\alpha = 0$, dashed line for T42, $\alpha = \pi/3$ and narrow solid line for T63, $\alpha = \pi/3$.

points. The T63 case shows a growth behavior similar to the rounding accumulation in the global zonal case. This is consistent with the larger orthonormality errors observed with higher resolution and smaller truncation errors expected with higher resolution. Additionally, the noise associated with the discrete sampling of the erroneous gravity waves is significantly smaller because the gravity wave amplitudes are smaller due to a more accurately approximated balance integral (for the initial state) on the T63 transform grid. The l_1, l_2, and l_∞ wind errors (not shown) for the T42 case are up to two orders of magnitude larger than the errors in Test Case 2 and show little growth during the 5-day integration period.

Unlike Test Case 2, the error distribution in Test Case 3 is clearly associated with the rotational pole and thus represents truncation error rather than the orthonormality error associated

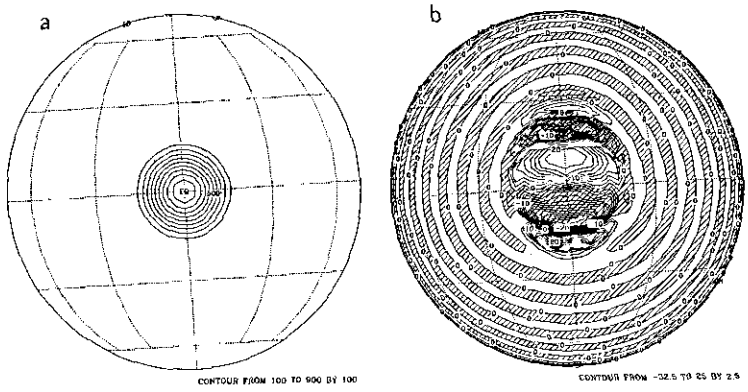

FIG. 4.3. Initial height field (a) and height field error (b) after one rotation for Test Case 1, where $\alpha = \pi/2 - 0.05$. Contour interval is 100 m for the field and 2.5 m for the error.

with the representational pole. Further evidence for this conclusion can be found in [8].

Test Case 1—Advection over the Pole

The remaining two test cases with analytic solutions present more of a challenge to the spectral transform method. Test Case 1, the advection of a cosine bell over the pole, is designed to test the advective component of a numerical scheme in isolation; i.e., it does not deal with the complete shallow water system. For this test case, a cosine bell is advected once around the sphere, directly around the equator ($\alpha = 0$), directly over the poles, and at slight angles to these two extremes, to expose any problems associated with asymmetries in a numerical scheme. The initial height field, which should be maintained throughout the course of one rotation is shown in Fig. 4.3a. For all rotation angles, α, the final height fields after one rotation (228 h or 864 time steps of 1200 s) are visibly indistinguishable from each other. Even the error fields for the different rotation angles ($\alpha = 0, 0.05, \pi/2 - 0.05$, and $\pi/2$) are extremely similar to each other, where the $\pi/2 - 0.05$ error distribution shown in Fig. 4.3b is representative. The error in Fig. 4.3b illustrates one of the principal shortcomings of the spectral transform method which is that it cannot maintain a flat field in the presence of other structures. In this case, error structures with alternating sign (arising from Gibbs phenomenon) are seen over the entire domain where the solution should be uniformly zero. This can be a serious deficiency for many geophysical applications. The l_1, l_2, and l_∞ error measures are shown in Figure 4.4 for the $\pi/2 - 0.05$ rotation angle using a T42 truncation and a 1200-s time step (once again, these curves are very similar for all four rotation angles, only the details of the high frequency noise component differ). These error estimates show a significant error associated with the initial representation of the cosine bell, followed by a systematic monotonic increase as the cosine bell is advected around the sphere.

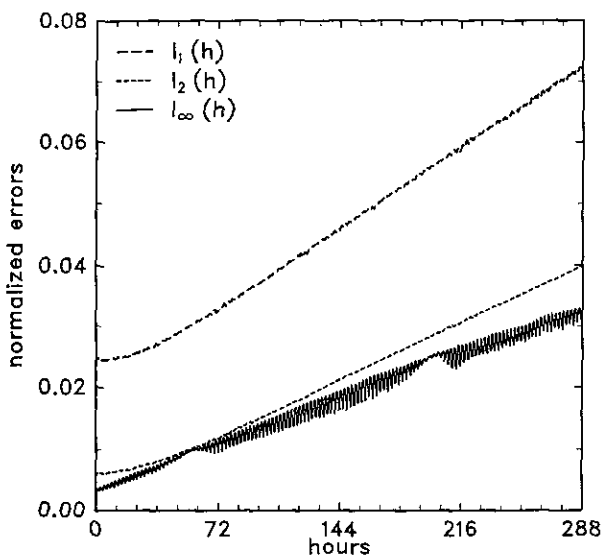

FIG. 4.4. l_1 (long dash), l_2 (short dash), and l_∞ (solid dash) errors versus time for Test Case 1 during one rotation where $\alpha = \pi/2 - 0.05$.

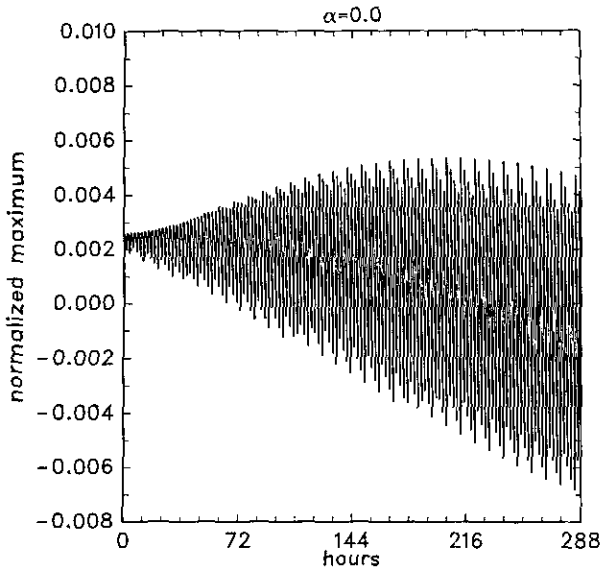

FIG. 4.5. Normalized maximum vs time for Test Case 1 during one rotation for $\alpha = 0.0$.

In addition to the global error estimates, this test case requests the time-dependent behavior of the normalized mean, variance, minimum, and maximum values in the height field. These curves are quite different in character for each of the four rotation angles and unfortunately are too numerous to present here. We refer the interested reader to [8] for additional details. In all cases the relative errors are very small, but they exhibit uniquely different low frequency modulations of some very high frequency behavior. By manipulating the analytic solution in various ways it can be demonstrated that the high frequency behavior seen in these figures is attributable to sampling the solution on a discrete grid. For example, an expanding envelope seen in the normalized maximum height error, shown in Fig. 4.5, is a consequence of sampling a solution with a very small phase error introduced by time truncation (and can be reproduced by sampling the *analytic* solution with a slight phase error). Thus, the running average represents the fundamental amplitude error. In all the error estimates for the $\pi/2 - 0.05$ and $\pi/2$ rotation angle solutions, there is the clear signature of a pole crossing. Once again, this is a consequence of sampling on the discrete grid, arising from a larger meridional grid interval at the polar cap.

Finally, in Fig. 4.6 we show the l_2 error estimates as a function of horizontal truncation for the $\pi/2 - 0.05$ rotation angle to illustrate the convergence properties of the solution. The time steps used were 600, 900, 600, and 450 s for the T42, T63, T106, and T170 truncations, respectively. These are the standard values listed in Section 2 with the exception of the T42 value. For purposes of this figure, the time step for the T42

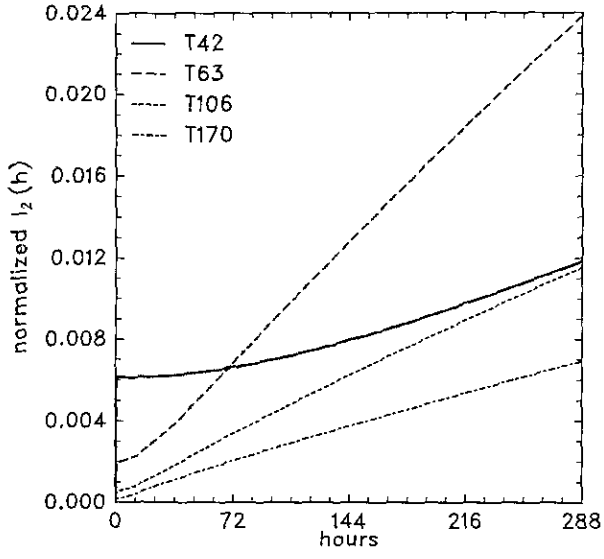

FIG. 4.6. l_2 height errors for Test Case 1 for T42, T63, T106, and T170 truncations with 600, 900, 600, and 450-s time steps, respectively.

solution was chosen to be the same as that used to generate the T106 solution, illustrating the role of the time truncation error. Error estimates with the standard T42 time step of 1200 seconds were shown earlier in Fig. 4.4. The curves in Fig. 4.6 show large differences in all measures at the initial state (associated with spectral truncation), with significantly smaller amplitudes at the higher resolutions. The growth of the error norms (i.e., the slope of these measures with respect to time) appears to be dominated by time truncation error. This can be clearly seen by comparing the T106 and T42 results with each other, since both were integrated using the sme time step. Additionally, comparison with the T42 case illustrated in Fig. 4.4 (using a 1200-s time step) shows faster growth with the longer time step. Thus, the selected time step is an important component in the error estimates reported for this test case.

Test Case 4—Forced Nonlinear Translating Low

The final test case in this analytical category, Test Case 4, the forced nonlinear system with a translating low, also presents a challenge to the spectral scheme in terms of representing the initial state and the analytic forcing. The horizontal scales of both the initial state and the forcing are considerably more complex than in the earlier test cases and are less accurately represented with comparable spectral truncations. This truncation error can be seen in all the error measures at $t = 0$ (e.g., see [8]), where modest improvements in horizontal resolution can yield significantly better results. A curious behavior is seen for the representation of the initial state using a T106 truncation, where all error estimates are worse than at T63. This is a consequence of the degree to which the basis functions are orthonormal, as discussed earlier. For practical purposes, how-

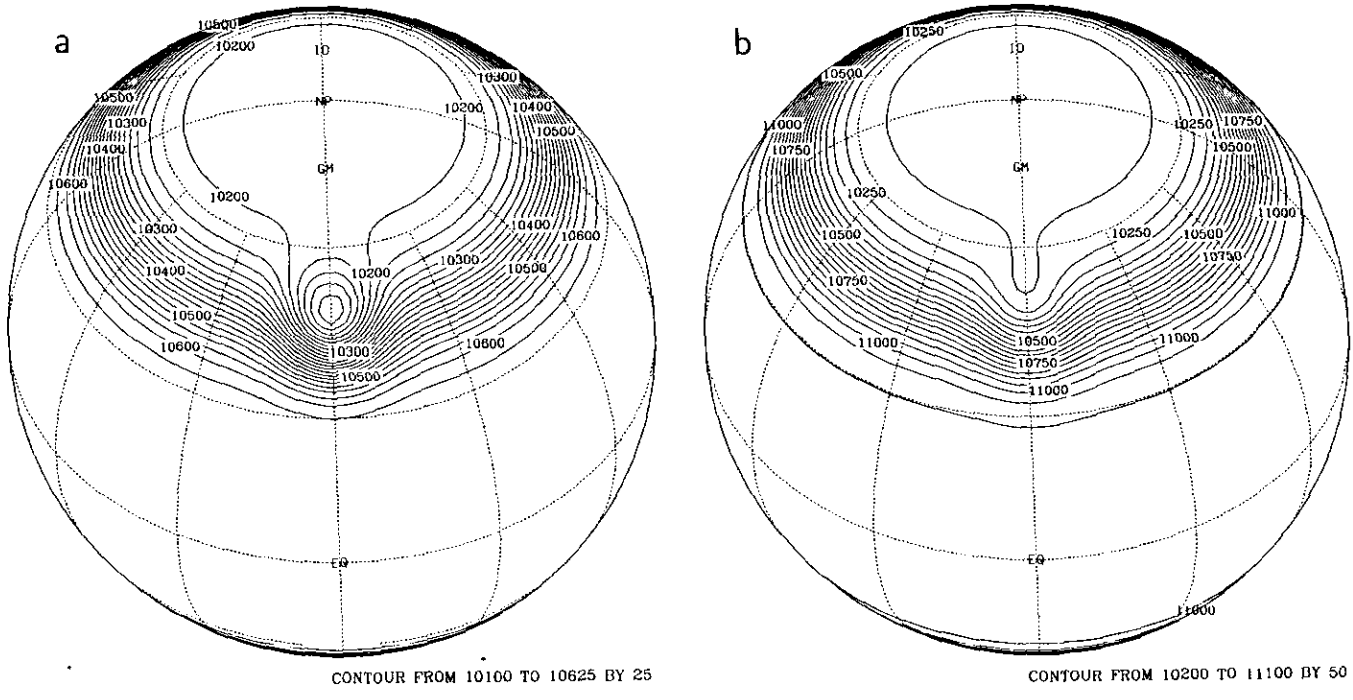

FIG. 4.7. Initial height field for Test Case 4 with (a) $u_0 = 20$ m/s and (b) $u_0 = 40$ m/s plotted on an orthographic projection centered at 45°N and the longitude of the trough in the analytic solution. Contour interval is (a) 25 m and (b) 50 m.

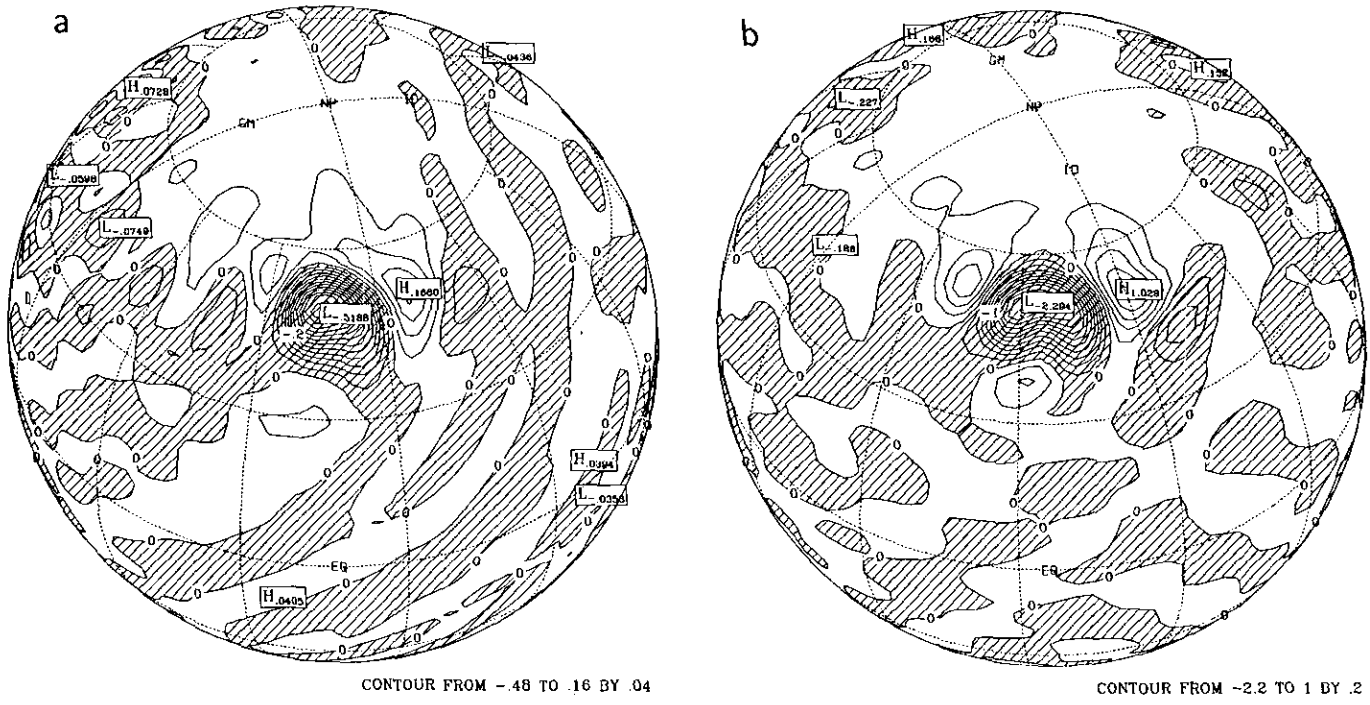

FIG. 4.8. Height errors at day 5 for Test Case 4 using a T42 truncation with (a) u_0 = 20 m/s and (b) u_0 = 40 m/s plotted on an orthographic projection centered at 45°N and the longitude of the trough in the analytic solution. The contour interval is (a) 0.04 m and (b) 0.2 m.

ever, the representation has already converged to machine accuracy using a T63 truncation.

Figure 4.7 shows the initial height field for the u_0 = 20 (left panel) and u_0 = 40 m/s (right panel) cases. After 5 days, these fields are indistinguishable from the initial condition. Figure 4.8 shows the structure of the corresponding height error at day 5 for Test Case 4 using a T42 truncation. Figure 4.9 presents the time evolution of the $l_2(h)$ error norms for the two cases. The high frequency temporal noise appearing in these error measures occurs because the initial data have not been properly initialized; i.e., the mass and momentum fields have been specified independently and the corresponding truncation errors result in very small imbalances contributing to gravity-wave activity. Another important source of this noise arises from discrete sampling of the solution on the Gaussian grid as seen in the earlier test cases.

The l_1 error in the height field (not shown) grows rapidly during the first day of integration, after which it grows monotonically, but at less than one-tenth the initial rate. A similar, although less exaggerated behavior is seen in the l_1 wind error. The growth in these error curves is predominantly attributable to time truncation error, although in the early stages of the integration it is also associated with the geostrophic adjustment process. For example, during the period of rapid l_1 error growth, the l_∞ error shows a rapid decrease, followed by a rebound, as the slowly forced mass and momentum fields come into a consistent internal balance.

As mentioned earlier, the errors for this test case are dominated by the time truncation component. In T42 integrations for which the discrete time step has been halved (not shown), the growth in all error estimates is reduced by nearly a factor of 4. Integrations using a T63 truncation but the same time

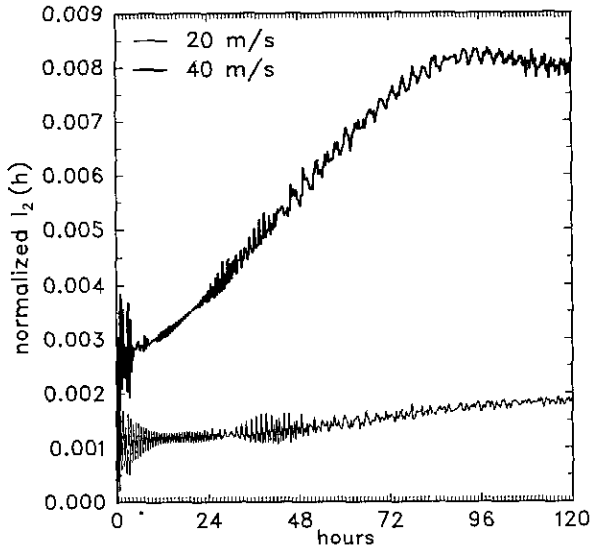

FIG. 4.9. l_2 height errors for Test Case 4 using a T42 truncation for u_0 = 20 and 40 m/s.

step as for the T42 truncation produce remarkably similar results in the global error estimates, although the detailed structure of the error distribution is noticeably different. The maximum departures are in the vicinity of the translating low pressure cell.

The l_2 and l_∞ errors in both the height and wind field generally show a monotonic increase in time after the initial adjustment, but begin to exhibit signs of a low frequency oscillation after about 4 days. This behavior is most apparent in the $u_0 = 40$ m/s case, for which all the error estimates are systematically larger than the $u_0 = 20$ m/s case (another indication of the dominance of time truncation error). We believe that this behavior is attributable to secondary nonlinearities associated with the growing inconsistency between the evolving state and the analytically specified forcing, seen initially as a phase error. One would expect this type of behavior to be more pronounced

$$h_s = h_{s_0}(1 - r/R), \tag{5.1}$$

where $h_{s_0} = 2000$ m, $R = \pi/9$, and $r^2 = \min[R^2, (\lambda - \lambda_c)^2 + (\theta - \theta_c)^2]$. The center is taken as $\lambda_c = 3\pi/2$ and $\theta_c = \pi/6$. A qualitative sense for the horizontal scale and location of the mountain feature can be gleaned from the error distributions shown in [8].

The representation of the mountain height and, thus, the depth of the fluid for this test case, is a challenge for the spectral scheme at all resolutions. Significant fluid depth errors occur initially in the vicinity of the mountain. These errors rapidly translate into local errors in the height of the fluid which are comparable in magnitude to the downstream errors that form during the integration. The height field for the T213 reference

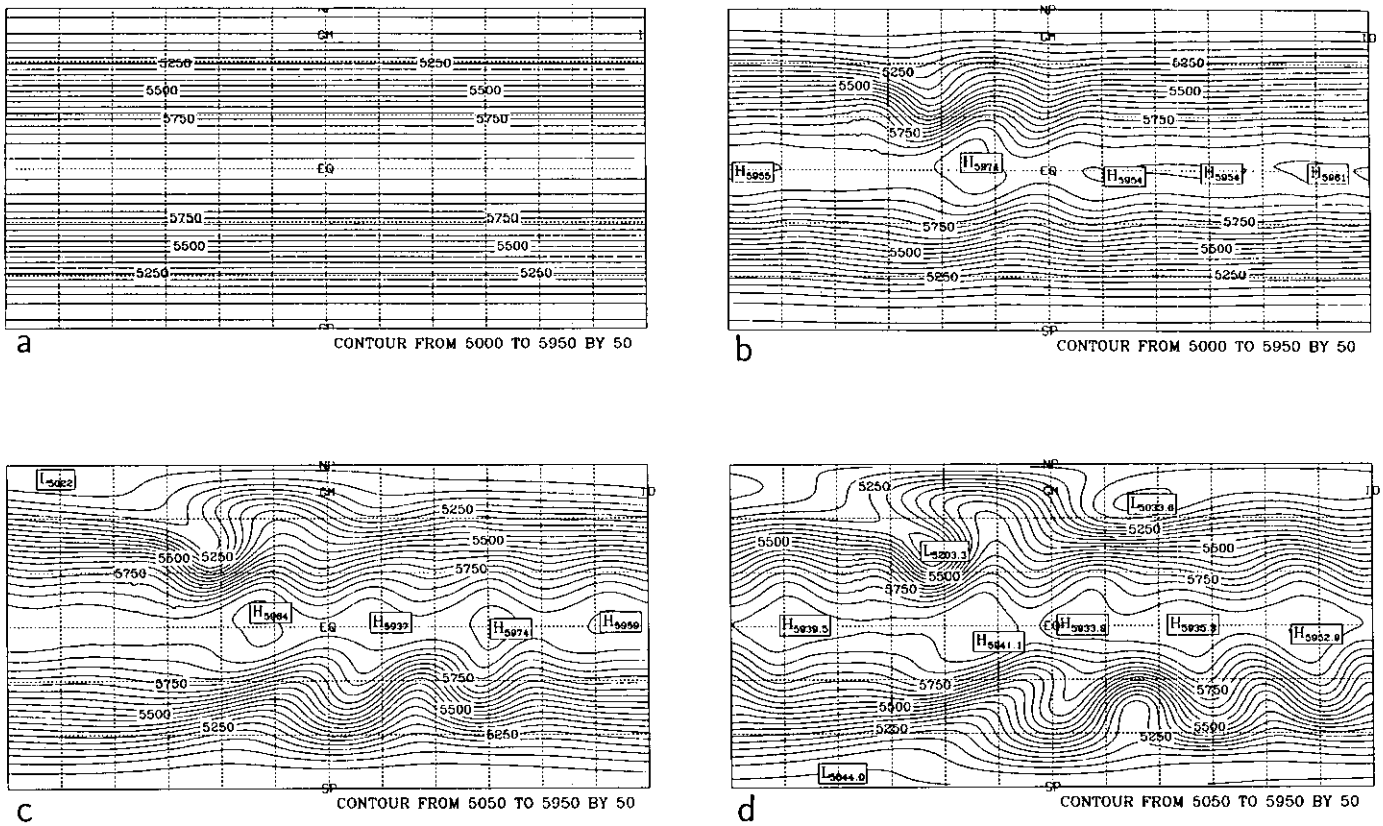

FIG. 5.1. T213 reference height solution for Test Case 5: (a) day 0; (b) day 5; (c) day 10; (d) day 15 on a cylindrical equidistant projection. The contour interval is 50 m.

growth where the T63 error estimates are modestly smaller than the T42 results.

Global integrals of mass and energy as a function of time, are shown in Fig. 5.3. Both resolutions exhibit comparable systematic increases in mass during the course of the integration, which is of the same order as machine rounding. Total energy decays as a consequence of internal dissipation, with an expectedly larger decay rate in the lower resolution result. The unnormalized integrals of relative vorticity and divergence, shown in Fig. 5.4, are reasonably well maintained (i.e., order machine roundoff), but begin to exhibit signs of a slowly amplifying low frequency oscillation after about 20 days (not shown).

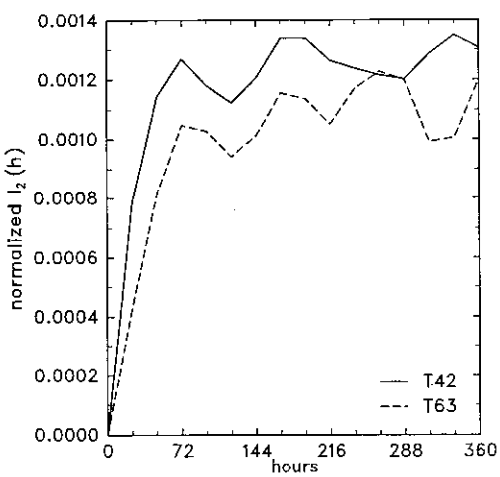

FIG. 5.2. I_2 height errors for Test Case 5 using T42 and T63 truncations.

Test Case 6—Rossby–Haurwitz Wave

The initial condition for Test Case 6, is a wavenumber-4 Rossby–Haurwitz wave. Rossby–Haurwitz waves are an ideal test of numerical solutions to the nonlinear nondivergent barotropic vorticity equation, since they represent exact analytic solutions. They are not closed-form solutions for the divergent barotropic system, however, and thus they cannot be regarded to be a rigorous test for the correct numerical solution of this system of equations. Nevertheless, they are a frequently used meteorological test and were included in the test case suite for this reason. Because no analytic solution is known, we must use a high resolution integration of the spectral model to generate a reference solution.

The representation of the initial condition for this test case is not a challenge to the spectral scheme. As the solution evolves,

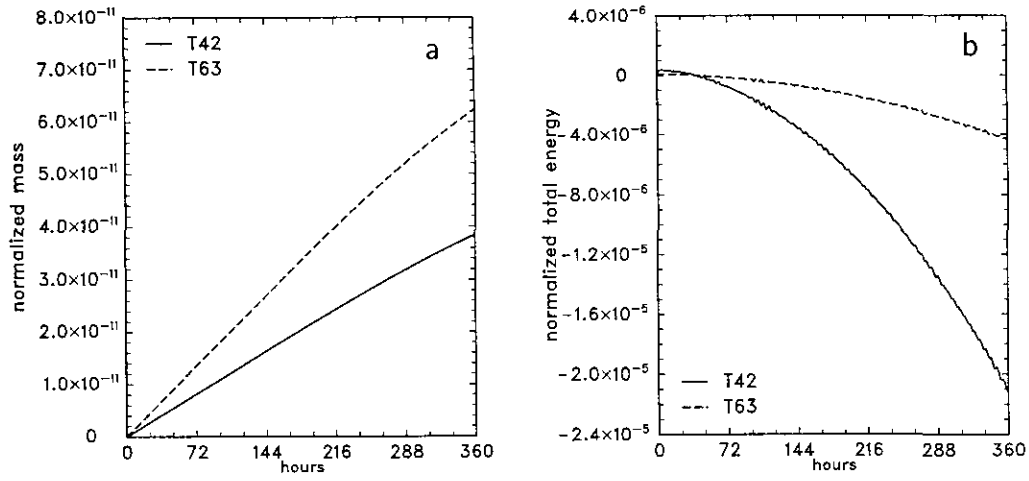

FIG. 5.3. Global integrals of (a) mass and (b) energy for Test Case 5 using T42 and T63 truncations.

however, the impact of horizontal resolution becomes more apparent, since the flow field does not maintain its initial structure. Figures 5.5a–d shows the height field for the T213 reference solution truncated to T106 and plotted on a T63 Gaussian grid for the initial state, day 1, day 7, and day 14, respectively. The time step for this integration is 180 s, which is smaller than the default listed in Section 3 (due to very strong winds associated with this test case), while the horizontal diffusion coefficient $K_4 = 8 \times 10^{12}\text{m}^4/\text{s}$ is the default value. As can be seen in these maps, there is a noticeable tendency for some sharpening of the mid-latitude troughs in the solution with a hint of some erosion of the tropical ridges. As mentioned earlier, the "errors" associated with the lower resolution integrations are a consequence of horizontal and temporal truncation errors, as well as the choice of the linear horizontal diffusion coefficient. To help quantify the role of horizontal diffusion in the high-resolution T213 reference solution, the diffusion term was eliminated in a second high-resolution integration. The l_2(h) difference in the two solutions is shown in Fig. 5.6. This measure illustrates that the first five days are essentially unaffected by the diffusion. After 14 days, this term leads to only a 0.08% l_2(h) difference in the solution and clearly plays a minor role in the reference solution results.

Figure 5.7 shows solutions of the height field for T42 (top) and T63 (bottom), along with the differences from the high-resolution reference solution at day 14. The corresponding l_2 error norms are shown in Fig. 5.8. The T42 and T63 truncations used time steps of 600 and 450 s, respectively, and diffusion coefficients of $5 \times 10^{15}\text{m}^4/\text{s}$ and $1 \times 10^{15}\text{m}^4/\text{s}$, respectively. At each of the two resolutions, we see similar structures in the error field with a general erosion of zonal and meridional gradients that increases with lower resolution. In general, the

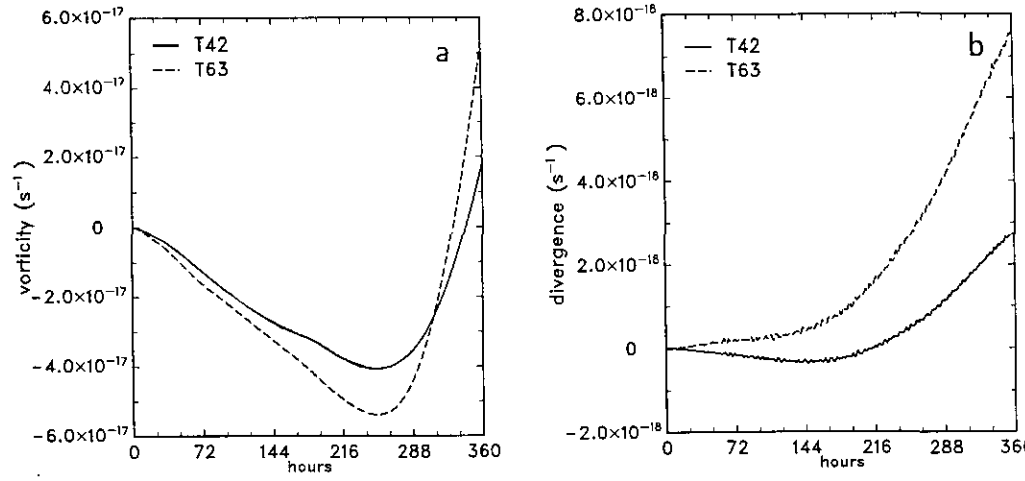

FIG. 5.4. Global integrals of (a) vorticity and (b) divergence for Test Case 5 using T42 and T63 truncations.

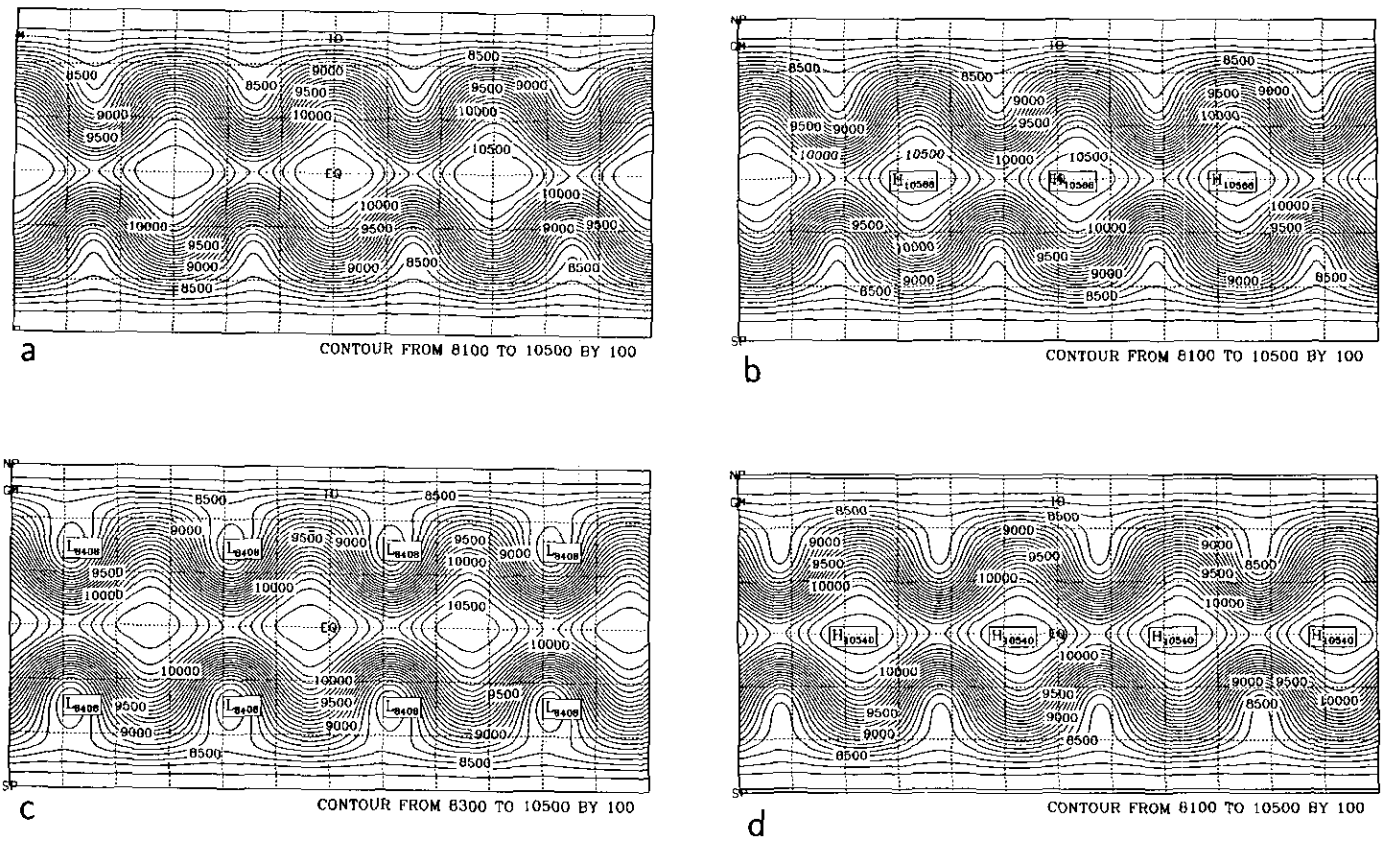

FIG. 5.5. T213 reference height solution for Test Case 6: (a) day 0; (b) day 1; (c) day 7; (d) day 14 on a cylindrical equidistant projection. The contour interval is 100 m.

T63 errors are about half the size of the errors exhibited by the T42 integration. In each case, the phase of the wave structure is very well represented.

With regard to conservation properties (Figs. 5.9 and 5.10) the T42 and T63 models do reasonably well. Both resolutions exhibit a comparable systematic relative increase in mass during the course of the integration, which is of the same order as machine rounding. Total energy decays as a result of internal dissipation, with a proportionally larger decay rate in the lower resolution result. The unnormalized integrals of relative vorticity and divergence are reasonably well maintained (i.e., order machine roundoff).

Integration of the T42 and T63 models with a 180-s time step suggests that time truncation is playing some role in the detailed structure of the error. A comparison of the height fields and differences with the T213 reference solution for the T42 run with a 180-s time step clearly shows the sensitivity. Although the general characteristics of the global error estimates (not shown) are not affected by the time step, the details are. The overall results, however, appear to be dominated primarily by spectral truncation and internal dissipation. The effect of horizontal diffusion has been examined using a T42 spectral

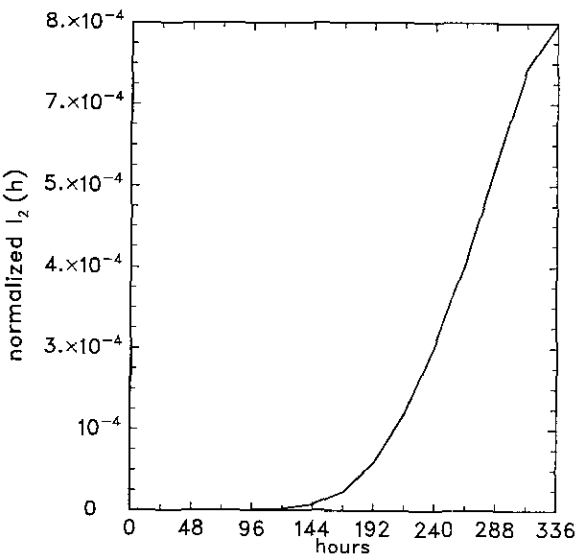

FIG. 5.6. l_2 height differences for T213

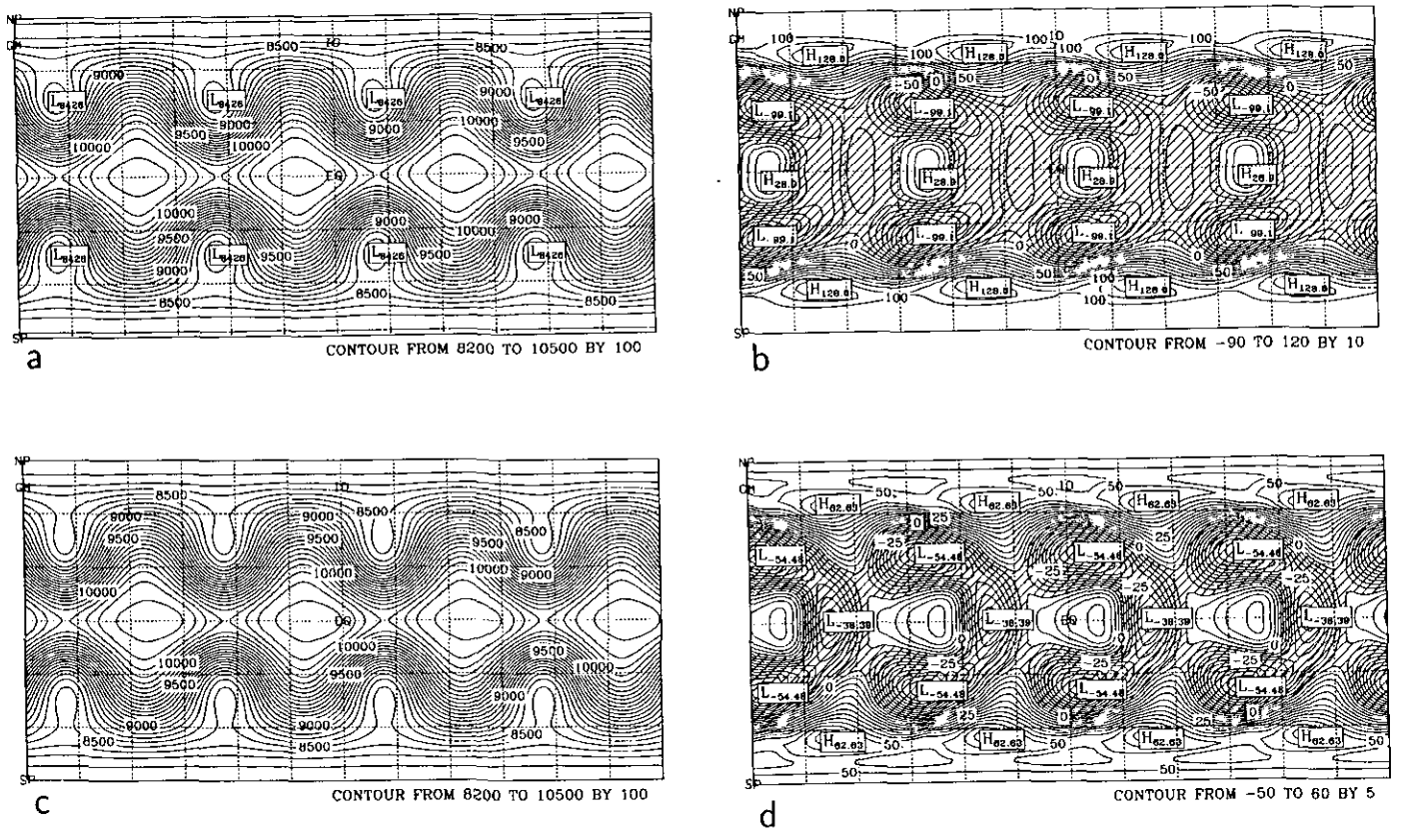

FIG. 5.7. Height fields at day 14 for Test Case 6 for (a) T42 and (c) T63 and differences with a reference solution for (b) T42 and (d) T63. The Contour intervals are: (a) 100 m; (c) 100 m; (b) 10 m; (d) 5 m.

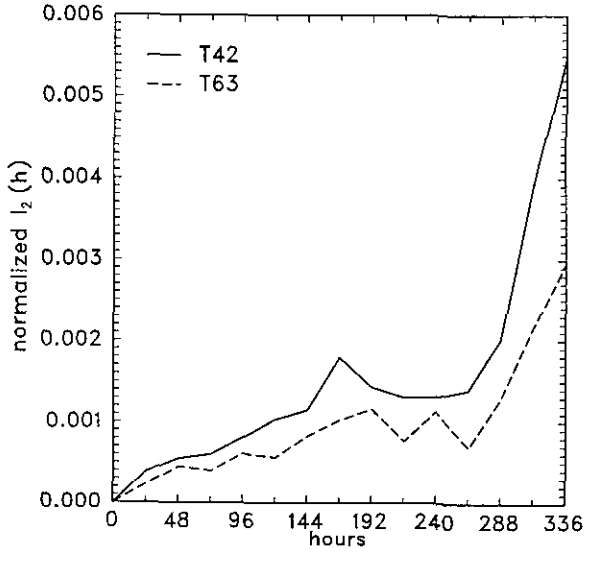

FIG. 5.8. l_2 height errors for Test Case 6 using T42 and T63 truncations.

time step. The overall character of the error distribution is noticeably different (although still quite small in amplitude) when the two solutions are compared (see [8]).

Finally, we have selected wavenumber 4 for this test case because it is empirically known to be a stable solution to the equations. Thus, small perturbations introduced by truncation error should not grow so rapidly over the 14-day integration period so as to produce a solution dominated in any way by such perturbations. However, since the flow structure does not maintain itself (as it would in the nondivergent barotropic system) and since the change in structure is a function of the horizontal resolution, one might ask how long the initial solution should be expected to remain stable. To address this question we have integrated the T42 version of the spectral model incorporating diffusion and a 600-s time step for a period of 60 days. The height field at 30 and 60 days clearly maintains its basic wavenumber-4 structure throughout the integration period, although the details of the simulated flow pattern change. Consequently, it is quite reasonable to assume that the true solution is nowhere near the point of breaking down after 14 days (the integration period proposed for the test case). Viable numerical methods should therefore be able to maintain the basic wavenumber-4 structure for the 14-day period at a minimum.

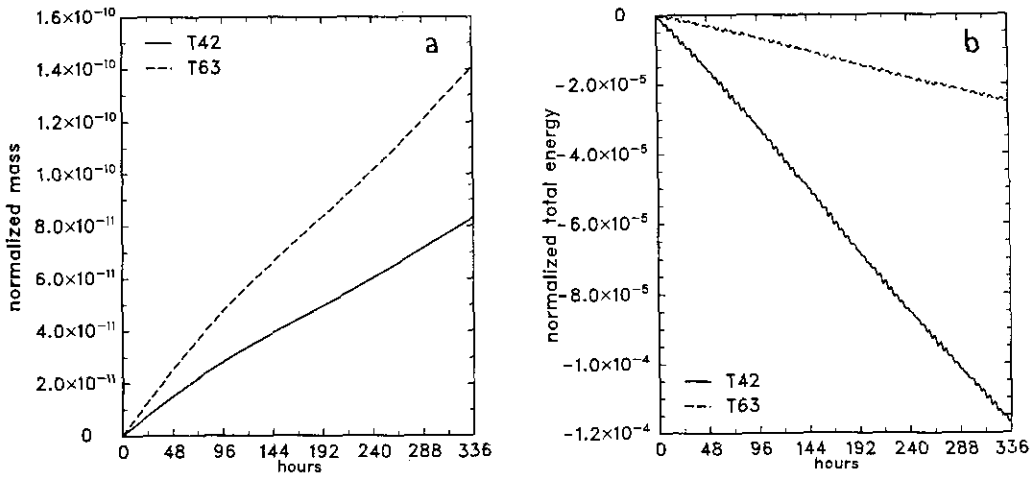

FIG. 5.9. Global average (a) mass and (b) energy for Test Case 6 using T42 and T63 truncations.

Test Case 7—Analyzed Initial Conditions

The integration of three analyzed 500-mb height and wind field initial conditions represents the remaining test case, Test Case 7. Since these cases make use of observed data, they must be initialized using a nonlinear normal mode initialization procedure as discussed in Section 3 and in [8]. As in the previous two test cases, horizontal diffusion was included for all numerical forecasts, where the implications of dissipation on the forecasts and reference solutions have been discussed earlier.

The l_2 height errors from forecasts using T42, T63, and T106 truncations are illustrated in Fig. 5.11. The short dashed curves are from the T42 forecasts, the solid curves are from the T63 forecasts, and the longer dashed curves are from the T106 forecasts. The circle line marker denotes the 21 Dec 1978 case, the square line marker denotes the 9 Jan 1979 case, and the triangle marker denotes the 16 Jan 1979 case. The relative behavior of the error norms in the three cases varies with the different resolutions. The l_1(h) and l_1(v) errors (not shown) improve with resolution as expected. As a general rule, the l_2(h) and l_2(v) errors improve with resolution. There is one example (see [8]), where a particular T63 forecast is not as good as a T42 forecast for a different case. For any given case, however, the l_2 error norms always decrease with increasing resolution. The l_∞(h) and l_∞(v) errors show a much larger spread with significant overlap among the resolutions. In the case of this error norm, increased resolution does not always result in a monotonic improvement in the forecast.

As discussed earlier in Section 3 (in the context of the high-resolution reference solution), the global integrals of mass were conserved to approximately 10 digits over the course of the

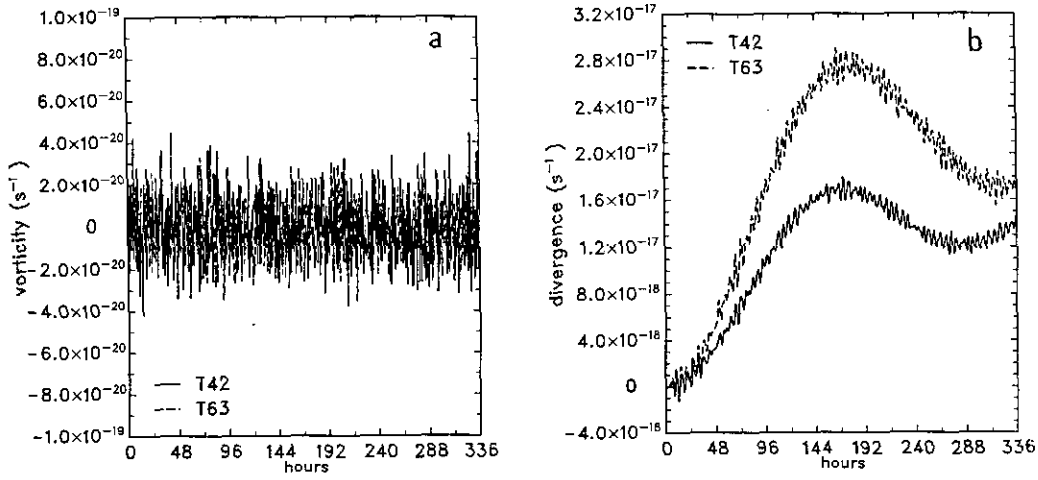

FIG. 5.10. Global average (a) vorticity and (b) divergence for Test Case 6 using T42 and T63 truncations.

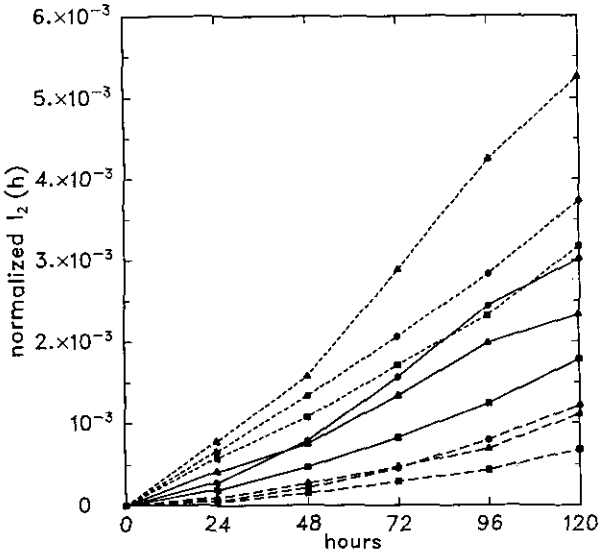

FIG. 5.11. l_2 height errors for Test Case 7 with short dash lines for T42, solid lines for T63, and long dash lines for T106. Circle line markers denote the 21 December 1978 case, squares for 9 January 1979, and triangles for 16 January 1979.

5-day forecasts. The global average vorticity, divergence, and energy generally behave as in the previous two test cases. The global average vorticity and divergence are generally better conserved for the lower resolution models, i.e., the T42 integration is marginally better than the T63 integration and the T63 results are noticeably better than the T106 results. Further comparison with the T213 reference integration shows that the T106 integration conserves these quantities better than the T213 simulation. This degradation in the degree of conservation is primarily attributable to the lack of discrete orthonormality in the Legendre functions as implemented in the spectral shallow water code (as discussed earlier in Section 3). The normalized global average total energy is conserved better with increased resolution, primarily associated with the decreased diffusion, as would be expected. Similar conservation improvements are seen in the T213 reference integration. The degree to which energy is conserved is case-dependent, where the relative conservation behavior of the three cases is basically the same at all resolutions.

Figure 5.12 presents a north polar stereographic map of the initialized height field for the 21 December 1978 case. For the purpose of the following discussion we include contour maps

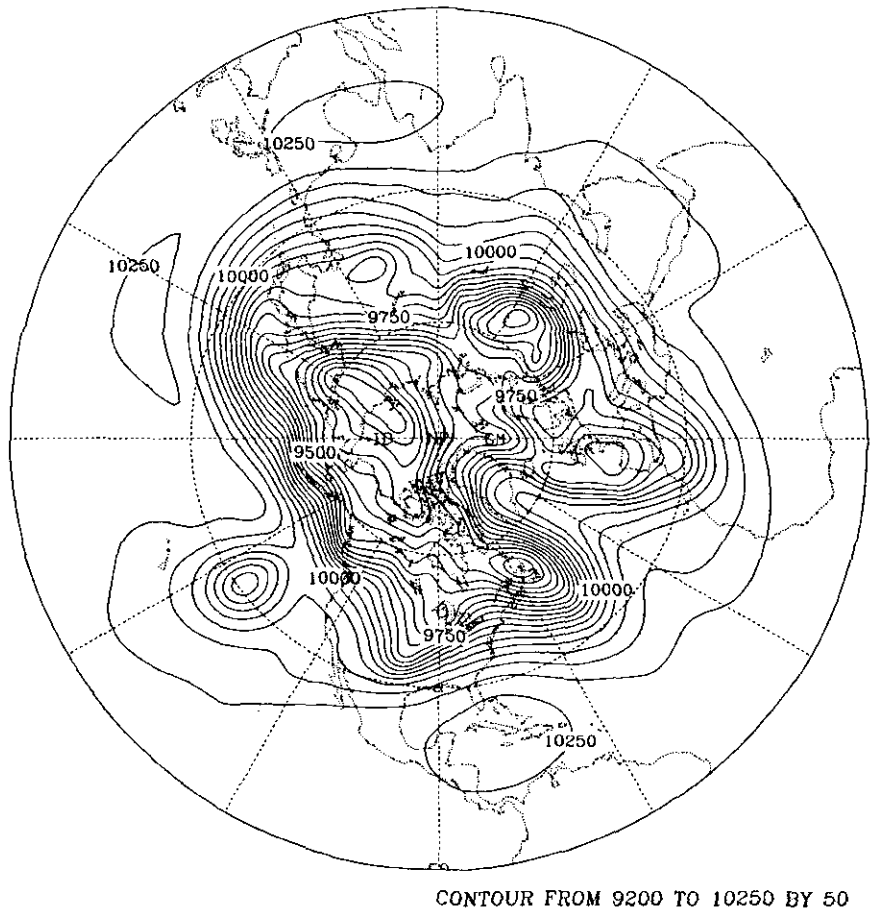

FIG. 5.12. Initial height field on a North polar stereographic projection for the 21 December 1978 case. Contour interval is 50 m.

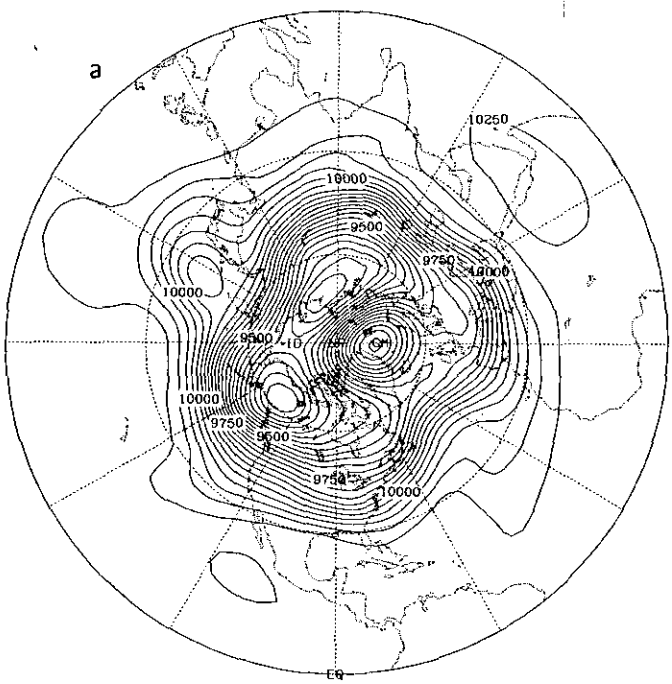

CONTOUR FROM 9100 TO 10250 BY 50

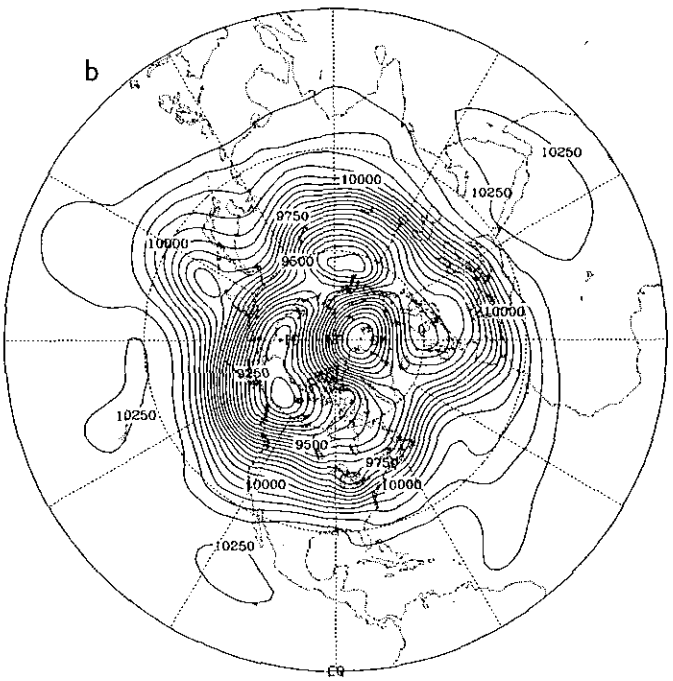

CONTOUR FROM 9100 TO 10250 BY 50

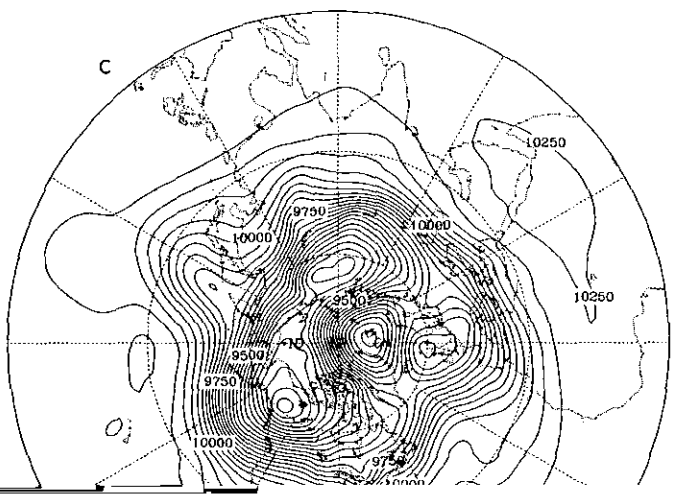

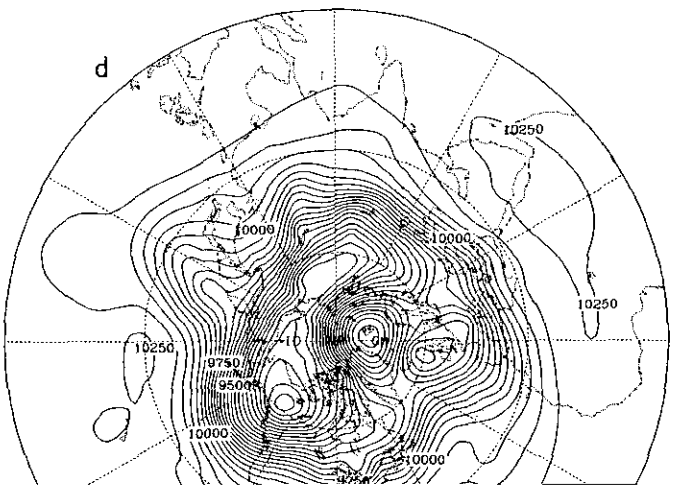

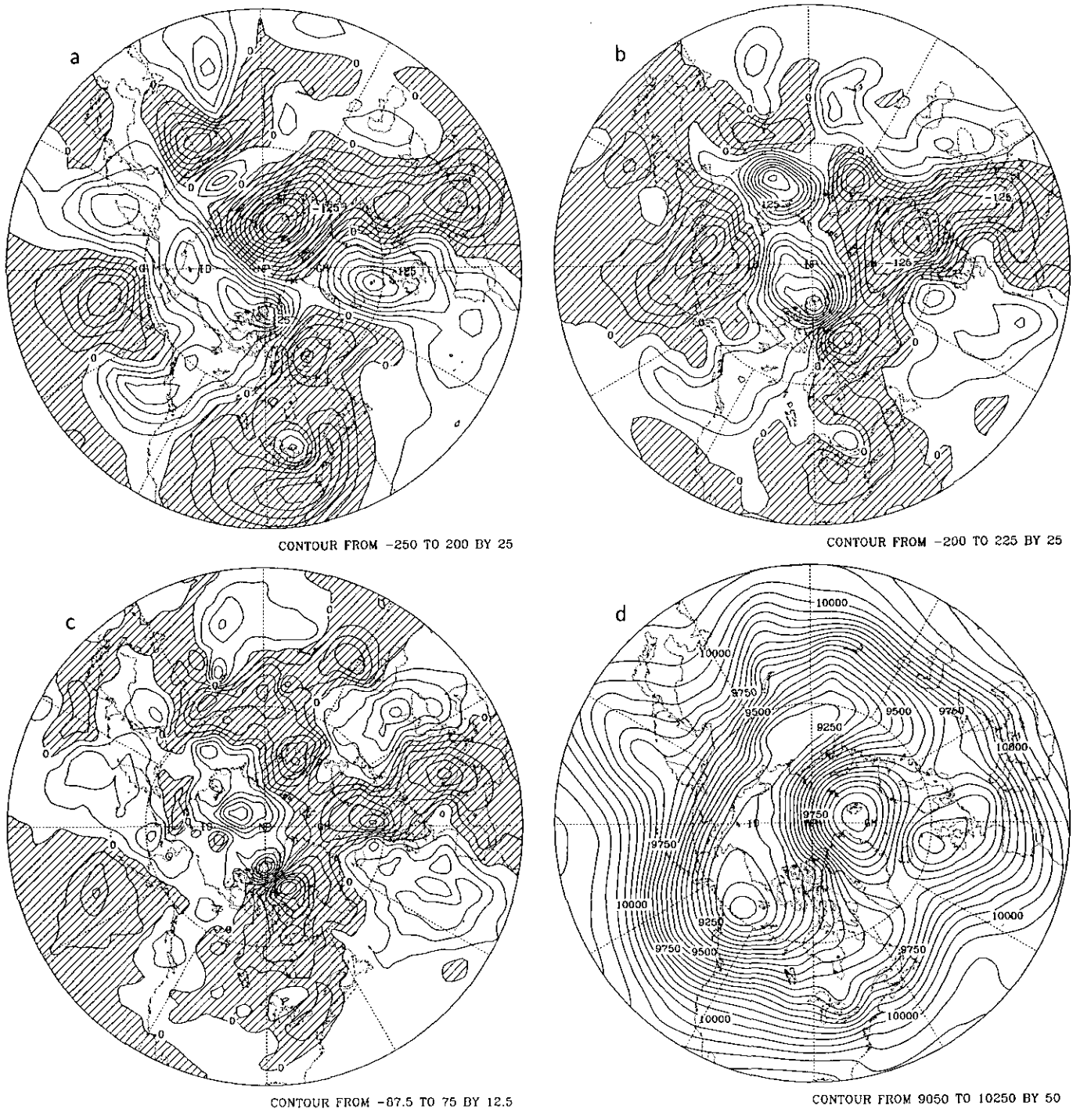

FIG. 5.14. Differences with reference solution of height field for day 5 of the 21 December 1978 case on a North polar stereographic projection: (a) T42; (b) T63; (c) T106; (d) reference solution. The contour intervals are (a) 25 m, (b) 25 m, (c) 12.5 m, and (d) 50 m.

little of interest equatorward of 30°. Note that the spatial scale of the error fields are comparable at all resolutions, where the local amplitude drops with improvements in horizontal resolution. The reference solution is from a T213 integration with diffusion coefficient $K_4 = 8.0 \times 10^{12}$ m^4/s and a 350-s time step. The contour interval is 50 m for the height fields and 25 m, 25 m, and 12.5 m for the T42, T63, and T106 errors, respectively.

Figure 5.15 shows the trace of the height field at the grid points closest to Boulder, Colorado (40°N, 105°W) for the 21

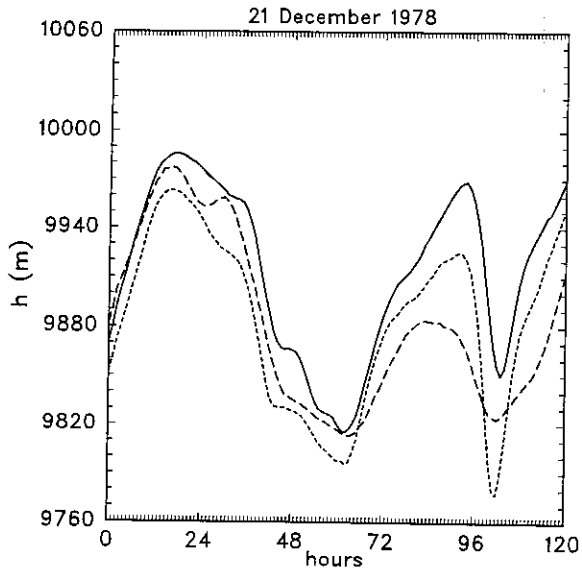

FIG. 5.15. Height field as a function of time at grid points closest to (40°N, 105°W) for T42 (short dash), T63 (solid), and T106 (long dash) using 21 December 1978 initial conditions.

Dec 1978 initial condition. The actual locations of the grid points are (40.77°N, 106.0°W) for the T42 truncation, (40.1°N, 105.0°W) for the T63 truncation, and (40.93°N, 104.63°W) for T106 truncation. The line codes for the different resolutions are the same as used earlier, with the short dash for T42, solid for T63, and long dash for T106. The data are plotted every hour rather than every iteration. Since in the T42 case this is an odd number of time steps, any significant $2\Delta t$ signal caused by even–odd splitting in the centered time differencing would appear in the graphs. There is no indication of such a signal. Similarly, the other resolutions also showed no $2\Delta t$ signal upon examination. The figures also indicate that high frequency gravity wave motion is not present in the forecasts. The three resolutions do not track each other identically, even initially, because the grid point locations are not identical. Even if they were identical, the grid values would likely differ, simply due to truncation differences. Nevertheless, solution similarity at the various resolutions is unmistakable.

CONCLUDING REMARKS

The spectral transform method is commonly adopted in Atmospheric General Circulation Modeling applications (e.g., numerical weather prediction and climate simulation). Since it is so widely used, it provides a benchmark against which alternative numerical approximations should be compared. This paper provides a summary of numerical solutions to the test case suite proposed by Williamson *et al.* [17] for the shallow water equations in spherical geometry. The solutions have been generated using the conventional spectral transform technique [6] to provide a basis for comparison. Complete details of the solution are provided in the technical report by Jakob *et al.* [8].

In almost all the test cases, the spectral transform method proves to be a highly accurate solution technique at resolutions typically associated with atmospheric general circulation models used to simulate the earth's climate. Two of the test cases (2 and 3) are trivial for the spectral transform method, in part because they involve structures consisting of the basis functions only. Clearly, these particular cases provide no practical information about the spectral transform method and alternative schemes do not have to do as well to be considered viable for practical atmospheric applications. The spectral transform method exhibits one undesirable characteristic for climate model application, which is the introduction of spurious wave structures in the solution. This characteristic is seen most clearly in Test Cases 1 and 5. Although this is not necessarily a problem in accurately simulating fluid flow, it becomes a serious problem in climate applications in which subgrid scale parameterizations are strongly dependent on the predicted large-scale state. The introduction of spurious wave structures can produce non-physical states such as negative water vapor mixing ratio [18]. In addition, it can also result in a strong, spurious modulation of the calculated forcing fields such as surface heat fluxes.

APPENDIX

The spectral transform shallow water model (STSWM) used to generate the solutions presented in this paper is coded in the Fortran 77 programming language [1] and is available via anonymous FTP from the authors. A more detailed description is available in electronic form from ftp.ucar.edu (IP address: 128.117.7.32) in the plain text file /chammp/shallow/docu/description.txt.

Reference solutions for Test Case 5 (zonal flow over an isolated mountain), Test Case 6 (Rossby–Haurwitz wave) and Test Case 7 (analyzed 500-mb height and wind field initial conditions) were computed using the STSWM, since the solutions to these test cases are not analytic. The model code was compiled using the Cray Fortran CFT77 compiler, version 5.0.4.1 and linked and executed under the UNICOS 6.1 operating system on a Cray Y-MP 8/864. Real and integer variables used a word length of 64 bits, which equals about 14 decimal digits accuracy for the mantissa of real variables. Further detail on how these reference solutions were obtained, along with measures of their uncertainty, are provided in Jakob *et al.* [8]. The solutions themselves are provided in the form of spectral expansion coefficients using the portable NetCDF data format. Fortran code to project these coefficients onto an arbitrary grid is also included. Instructions on how to obtain the solutions and code can be found in the plain text file /chammp/shallow/docu/refsol.txt. The reference solutions and codes are also available at Oak Ridge National Laboratory. A

list of available material can be obtained by mailing "send index from chammp" to netlib@ornl.gov. Instructions on how to obtain the solutions and code can be obtained by mailing "send REDME from chammp" to netlib@ornl.gov. Difficulties in accessing the files at NCAR should be reported to the NCAR computer consulting office at 303-497-1278 (email: consult1@ncar.ucar.edu). Difficulties in accessing files at ORNL should be reported electronically to bbd@ornl.gov. Software bugs, along with suggested fixes, should be reported electronically to stswm@ncar.ucar.edu. Copies of the technical report [8], which contains complete details of all the solutions to the test cases summarized here, may be obtained from Hack or Williamson at NCAR (jhack@ncar.ucar.edu; wmson@ncar.ucar.edu).

ACKNOWLEDGMENTS

We thank Andy van Tuyle for providing the nonlinear normal mode initialization code for the shallow water equations. We also thank John Truesdale for his help in completing higher resolution integrations that are discussed in the revised manuscript. This work was partially supported by the Computer Hardware Advanced Mathematics Model Physics (CHAMMP) Program which is administered by the Office of Energy Research under the Office of Health and Environmental Research in the Department of Energy Environmental Sciences Division.

REFERENCES

1. ANSI X3J3, 1978: *Programming Language FORTRAN Standard* (American National Standards Institute, New York, 1978).
2. W. Bourke, B. McAvaney, K. Puri, and R. Thurling, *Methods in Computational Physics* Vol. 17, General Circulation Models of the Atmosphere (Academic Press, New York/London, 1977), p. 267.
3. E. Eliasen, B. Machenhauer, and E. Rasmussen, Report No. 2, Institut for Teoretisk Meteorologi, University of Copenhagen, 1970 (unpublished).
4. R. M. Errico, NCAR Technical Note NCAR/TN-277+STR, NTIS PB89-113989/AS, 1987 (unpublished).
5. R. M. Errico and B. E. Eaton, NCAR Technical Note, NCAR/TN-303+IA, NTIS PB88-171814/AS, 1987 (unpublished).
6. J. J. Hack and R. Jakob, NCAR Technical Note NCAR/TN-343+STR, NTIS PB92-155258, 1992 (unpublished).
7. J. J. Hack, B. A. Boville, B. P. Briegleb, J. T. Kiehl, P. J. Rasch, and D. L. Williamson, NCAR Technical Note NCAR/TN-382+STR, NTIS PB93-221802, 1993 (unpublished).
8. R. Jakob, J. J. Hack, and D. L. Williamson, NCAR Technical Note NCAR/TN-388+STR, NTIS PB93-202729, 1993 (unpublished).
9. R. Jakob, Ph.D. thesis, University of Colorado, Boulder, Colorado, 1993 (unpublished).
10. S. A. Orszag, *J. Atmos. Sci.* **27,** 890 (1970).
11. B. Machenhauer, 1979: "The Spectral Method," in *Numerical Methods Used in Atmospheric Models,* GARP Publication Series Vol. 17 (World Meteorological Organization, Geneva, Switzerland, 1979), p. 121.
12. S. Matsumoto, *J. Meteorol. Soc. Japan* **39,** 18 (1961).
13. C. G. Rossby, *J. Marine Res.* **1,** 239 (1938).
14. C. Temperton, *J. Comput. Phys.* **52,** 340 (1983).
15. K. E. Trenberth and J. G. Olson, NCAR Tech. Note NCAR/TN-300+STR, NTIS PB88-178165/AS, 12 fiche, 1988 (unpublished).
16. D. L. Williamson, J. T. Kiehl, V. Ramanathan, R. E. Dickinson, and J. J. Hack, NCAR Technical Note NCAR/TN-285+STR, NTIS PB87-203782/AS, (1987).
17. D. L. Williamson, J. B. Drake, J. J. Hack, R. Jakob, and P. N. Swarztrauber, *J. Comput. Phys.* **102,** 211 (1992).
18. D. L. Williamson and P. J. Rasch, *Tellus* **46A,** 34 (1994).